Title
Cryo-EM structures of the TMEM16A calcium-activated chloride channel

Journal
Nature, 552(7685)

ISSN
0028-0836

Authors
Dang, Shangyu
Feng, Shengjie
Tien, Jason
et al.

Publication Date
2017-12-01

DOI
10.1038/nature25024

Peer reviewed

Published in final edited form as:

Nature. 2017 December 21; 552(7685): 426–429. doi:10.1038/nature25024.

Cryo-EM structures of the TMEM16A calcium-activated chloride channel

Shangyu Dang[1,*], **Shengjie Feng**[2,*], **Jason Tien**[2,*], **Christian J. Peters**[2], **David Bulkley**[1], **Marco Lolicato**[3], **Jianhua Zhao**[1], **Kathrin Zuberbühler**[4], **Wenlei Ye**[2], **Lijun Qi**[2], **Tingxu Chen**[2], **Charles S. Craik**[4], **Yuh Nung Jan**[1,2,5], **Daniel L. Minor Jr.**[1,2,3,6,7], **Yifan Cheng**[1,5,§], and **Lily Yeh Jan**[1,2,5,§]

[1]Department of Biochemistry and Biophysics, University of California, San Francisco, California 94158, USA

[2]Department of Physiology, University of California, San Francisco, California 94158, USA

[3]Cardiovascular Research Institute, University of California, San Francisco, California 94158, USA

[4]Department of Pharmaceutical Chemistry, University of California, San Francisco, California 94158, USA

[5]Howard Hughes Medical Institute, University of California, San Francisco, California 94158, USA

[6]Department of Cellular and Molecular Pharmacology, University of California, San Francisco, California 94158, USA

[7]Molecular Biophysics and Integrated Bio-imaging Division, Lawrence Berkeley National Laboratory, Berkeley, California 94720, USA

Calcium-activated chloride channels (CaCCs) encoded by TMEM16A[1–3] control neuronal signaling, smooth muscle contraction, airway and exocrine gland secretion, and rhythmic movements of the gastrointestinal system[4–7]. To understand how CaCCs mediate and control

§Correspondence and requests for materials should be addressed to Y.C. (ycheng@ucsf.edu) and L.Y.J. (lily.jan@ucsf.edu).
*These authors contributed equally to this work.
Correspondence and requests for materials should be addressed to Y.C. (ycheng@ucsf.edu) and L.Y.J. (Lily.Jan@ucsf.edu).

Data Availability

Cryo-EM density maps of TMEM16A have been deposited to the Electron Microscopy Data Bank (EMDB) under the accession number EMD-7095 and EMD-7096. Particle image stack after motion correction related to TMEM16A has been deposited in the Electron Microscopy Public Image Archive (http://www.ebi.ac.uk/pdbe/emdb/empiar/) under accession number EMPIAR-10123 for nanodisc-reconstituted TMEM16A and EMPIAR-10124 for LMNG-solubilized TMEM16A. Atomic coordinates for TMEM16A have been deposited in the Protein Data Bank (PDB) under the accession number 6BGI and 6BGJ. All electrophysiological data generated or analyzed during this study are included in this published article. All other data are available from the corresponding authors upon reasonable request.

Author Contributions

S.D., S.F. and J.T. designed and performed most of the biochemical and cryo-EM experiments. C.J.P., J.T., W.Y., L.Q. and T.X. performed mutagenesis and electrophysiology experiments. K.Z. and J.T. isolated the Fab that binds TMEM16A, M.L. and J.T. performed systematic screens of deletion constructs and purification schemes. S.D., D.B., M.L. and S.F. built *de novo* models. J.Z. developed methods to calculate directional resolution. L.Y.J., Y.N.J., D.L.M., C.S.C. and Y.C. supervised experiments and data analysis. All authors contributed to manuscript preparations.

The authors declare no competing financial interest.

anion permeation to fulfill these physiological functions, knowledge of the mammalian TMEM16A structure and identification of its pore-lining residues is essential. TMEM16A forms a dimer with two pores[8,9]. Thus far, CaCC structural analyses relied on homology modeling of a fungal homolog nhTMEM16 that functions primarily as a lipid scramblase[10–12] and subnanometer-resolution electron cryo-microscopy (cryo-EM)[12]. Here, we present *de novo* atomic structures of the transmembrane domains of mouse TMEM16A in nanodiscs and in lauryl maltose neopentyl glycol (LMNG) as determined by single-particle cryo-EM. These structures reveal the ion permeation pore and represent different functional states. The LMNG structure has one Ca^{2+} ion resolved within each monomer with a constricted pore, likely corresponding to a closed state because CaCC with single Ca^{2+} occupancy requires membrane depolarization to open[13]. The nanodisc structure has two Ca^{2+} ions per monomer and its pore in a closed conformation likely reflects channel rundown, a gradual loss of channel activity following prolonged CaCC activation in 1 mM Ca^{2+}. Structure-based mutagenesis and electrophysiological studies identified ten residues distributed along the pore that interact with permeant anions and affect anion selectivity as well as seven pore-lining residues that cluster near pore constrictions and regulate channel gating. Together, these data clarify the basis of CaCC anion conduction.

Our screen of deletion constructs of the mouse TMEM16A splice variant[1] that contains exon ‘a’ but not exons ‘b-d’ identified a C-terminally truncated mutant with high expression and stability (Extended Data Fig. 1a) and channel function (Extended Data Fig. 1b). Its increased Ca^{2+} sensitivity is reminiscent of gating changes observed in other TMEM16A truncation mutants[14,15]. Reducing negatively charged lipids via poly-L-lysine (PLL) caused desensitization by reducing Ca^{2+} sensitivity without altering the plateau current (Extended Data Fig. 1c). This truncated TMEM16A including amino acids 1–903 was purified in detergent followed by reconstitution into lipid nanodiscs (Extended Data Fig. 1d) or kept solubilized in LMNG (Extended Data Fig. 1h) for further analyses. N-[4-(7-diethylamino-4-methyl-3-coumarinyl)phenyl]maleimide (CPM) assay[16,17] revealed a similar melting temperature (T_m) for Ca^{2+}-free TMEM16A while stepwise increase of Ca^{2+} concentration caused T_m to gradually increase for TMEM16A in nanodisc but not for LMNG-solubilized TMEM16A (Extended Data Fig. 1e, i); this stabilizing effect of Ca^{2+} reached plateau at ~1 μM Ca^{2+} (Extended Data Fig. 1e), as did channel activation (Extended Data Fig. 1b). The CPM assay thus revealed that TMEM16A in nanodiscs or LMNG differ in their Ca^{2+} binding characteristics.

Negative stain electron microscopy (EM) of LMNG-solubilized TMEM16A and dodecylmaltoside (DDM):cholesterol hemisuccinate (CHS)-solubilized TMEM16A reconstituted into lipid nanodiscs revealed homogeneous preparations suitable for high resolution structural studies (Extended Data Fig. 1f, g, j, k). Using single-particle cryo-EM we determined the structures of TMEM16A to better than 4 Å nominal resolutions (Extended Data Fig. 2, 3, 4b). Local resolution analysis showed that the core transmembrane domains have the highest (better than 4 Å) resolution and the extracellular and cytoplasmic domains have the poorest (Extended Data Fig. 2f, 3f), suggesting conformational flexibility of these regions. The resolution of the LMNG-solubilized TMEM16A reconstruction is anisotropic because images of particles oriented along certain axes were lacking (Extended Data Fig. 3c, h, i). Because the missing views are within a small angular range, there is no

distortion regarding the definition of the transmembrane helices with respect to the membrane. The anisotropy is considerably reduced by adding particles from a dataset in which a monoclonal fragment of antigen binding (Fab) isolated from a human naïve Fab phage library[18,19] is bound to TMEM16A (Extended Data Fig. 3b, h, i). The final density maps allowed reliable assignment of most of the side chains in all ten transmembrane segments and enabled building *de novo* atomic models of the transmembrane segments of dimeric TMEM16A in both nanodisc and LMNG (Fig. 1a, b; Extended Data Fig. 4a, c, d, 5a–f). Cross-validation between the atomic model and the density maps of the transmembrane domains suggested that the average resolutions are around 4 Å (Extended Data Fig. 2g, 3g). The nanodisc-reconstituted TMEM16A is structurally similar to the subnanometer-resolution structure of digitonin-solubilized TMEM16A[12] but missing part of the C-terminal cytoplasmic domain owing to the truncation construct used in our study (Extended Data Fig. 5g–i).

To locate the pore, we used the HOLE program[20] to delineate potential water-filled profiles in these structures. By testing whether anion selectivity could be altered by mutations of residues lining the potential pore within each monomer or the potential pore at the dimer interface that is associated with lipids, we identified the pore surrounded by transmembrane helices TM3–8 (Fig. 1c–e and Extended Data Fig. 6d). This pore is not exposed to the lipid bilayer as proposed[21–24]. Similar to a previous study[12], our cryo-EM studies revealed a pore too narrow for the passage of permeant anions. It remains possible that some open conformation of the pore is partly lined by lipids.

A comparison of nanodisc-reconstituted and LMNG-solubilized TMEM16A density maps (Fig. 2a, b) revealed differences primarily in the positions and orientations of TM3, TM4, and TM6 (Fig. 2c–f; Extended Data Fig. 7a–f). These pore-lining helices in the TMEM16A channel are also displaced noticeably from the positions of the equivalent helices of the nhTMEM16A lipid scramblase[10]. We found some helical distortions in the nanodisc-reconstituted TMEM16A starting from G640 and extending towards the lower part of TM6 (Extended Data Fig. 4a, 7a, b). In the LMNG reconstruction, the lower part of the TM6 could not be resolved beyond G640 (Extended Data Fig. 4a, 7d, e). These observations are in agreement with mutagenesis studies implicating G640 as a flexible hinge that affects channel gating[13]. Additionally, the two structures differ in the orientation of TM3 and in the arrangement of the TM5-TM6 loop that is near the pore entrance and harbors K599 and R617 important for anion selectivity[25], and the TM9-TM10 loop that harbors R784 important for anion selectivity[25] and packs against the TM5-TM6 loop (Extended Data Fig. 7g–l). We observed densities consistent with the presence of ordered lipids near the dimer interface but not near the pore of both nanodisc-reconstituted and LMNG-solubilized TMEM16A (Fig. 1a; Extended Data Fig. 7b, c, e, f). And the number of ordered lipids observed in the nanodisc structure is greater than that in the LMNG structure. It is possible that lipids may stabilize TMEM16A in the more native environment of nanodiscs.

These two structures showed a surprising difference near the putative Ca^{2+} binding sites even though both structures were determined in the presence of 1 mM calcium. Consistent with previous studies[10,26,27], the acidic residues E650, E698, E701, E730 and D734 group together to form two Ca^{2+} binding sites in nanodisc-reconstructed TMEM16A (Fig. 2g, h).

Comparisons of the maps and models suggest that these residues are well organized in nanodisc-reconstructed TMEM16A, but less so in LMNG-solubilized TMEM16A (Fig. 2h, i). The difference maps between the experimental map and the map from the refined structure that do not contain Ca^{2+} ions showed a clear omit density that we assigned as a bound Ca^{2+} ion, for LMNG-solubilized TMEM16 at σ = 13 and for nanodisc-reconstituted TMEM16A at σ = 8. The location of this bound Ca^{2+} ion matches well with one of the two bound Ca^{2+} ions in the crystal structure of nhTMEM16A[10]. In the nanodisc structure, there is another omit density (σ = 10) nearby that may correspond to the second bound Ca^{2+} ion (Fig. 2h). In contrast, in the LMNG structure, no other significant omit density was found nearby, suggesting there is only one Ca^{2+} ion bound (Fig. 2h). Notably, E650 on the lower half of TM6 is not resolved in LMNG-solubilized TMEM16A (Fig. 2h; Extended Data Fig. 4a, 7d). Our mutagenesis studies showing that alanine substitution of E650 raises the Ca^{2+} concentration for half maximal activation (EC_{50}) and reduces the Hill coefficient from two to one[13,26] indicate that this residue in TM6 is critical for Ca^{2+} binding. It is therefore understandable that the more flexible TM6 harboring E650 results in partial Ca^{2+} occupancy of LMNG-solubilized TMEM16A (Fig. 2h, i), raising the possibility that some of the conformational differences between the two structures could reflect different channel conformations. It appears that the native-like lipid environment of nanodiscs allowed stabilization of TM6 so that two Ca^{2+} ions can be fully coordinated by their binding sites (Fig. 2g, h).

Based on our structures (see Extended Data Fig. 8 for structural determination details), mutagenesis of residues lining the pore revealed that a subset of these residues affected anion selectivity (Fig. 3a–c). Besides R511 on TM3 and K599 on the TM5-TM6 loop important for anion selectivity[25], and K584 on TM5 that partially accounts for the selectivity for anions over cations[28] (Fig. 3b), we tested alanine substitutions of 24 other pore-lining residues including N542 and D550 on TM4, N587 and V595 on TM5, Q705 and F712 on TM7, and S635 on TM6 (Fig. 3a, b and Extended Data Fig. 6d). The permeability ratios determined by replacing external Cl^- with I^- or SCN^- were reduced by 40% by S635A but increased by 40–130% by the other six mutations (Fig. 3d–f). Whereas the side chains of Q705 and F712 do not appear to be pointing into the pore, it remains an open question whether they may reorient and face the pore as the channel opens. These ten pore-lining residues identified thus far for their roles in anion selectivity (Fig. 3c) may reflect an extended selectivity filter, or multiple pore regions for permeant ion interactions.

We noticed narrow constrictions of the pore of LMNG-solubilized TMEM16A (Fig. 4a–c), likely representing a stable closed conformation. To test whether residues facing the pore affect channel gating possibly by altering the relative stability of the open versus closed states, we examined alanine substitutions of 21 residues including N542 and I546 on TM4, Y589 and I592 on TM5, and F708 on TM7. These five alanine mutations increased the apparent Ca^{2+} sensitivity whereas alanine substitution of V595 on TM5 and L639 on TM6 decreased the apparent Ca^{2+} sensitivity (Fig. 4d–f and Extended Data Fig. 9c). In contrast to the pore-lining residues important for anion selectivity that are spread over more than 25 Å along the length of the pore (Fig. 3c), these seven residues affecting the Ca^{2+} dependence of channel activation are all located within ~10 Å from the pore constrictions (Fig. 4c),

indicating that these residues at the constricted pore influence the stability of the channel conformation important for gating.

TMEM16A-CaCC likely have multiple open states[2,13] and closed states[13] (Fig. 5a). With the same anion concentration on both sides of the membrane, occupancy of the first Ca^{2+} binding site allows the channel to open when the membrane potential is depolarized to positive values[13], whereas CaCC with double Ca^{2+} occupancy activates in a voltage independent manner[13]. The currents conducted by the C-terminally truncated TMEM16A also displayed voltage dependence at 30 nM Ca^{2+} but not 1 mM Ca^{2+} (Fig. 5b). Given the single Ca^{2+} occupancy of TMEM16A in LMNG, this structure is in a closed conformation probably because of the lack of depolarization. Moreover, we found that the K584Q mutation altered the ion selectivity in low but not high Ca^{2+} (Extended Data Fig. 9a, b), suggestive of multiple open states with differences in the permeation pathway[2] – a finding of potential relevance to the different mutagenesis results[8,9,28] regarding this pore-lining residue (Fig. 3a–c). The nanodisc-reconstituted TMEM16A structure likely corresponds to a closed conformation due to channel rundown following prolonged activation in 1 mM Ca^{2+} (Fig. 5c–e)[12]. Intrigued by the involvement of the hydrophobic V595 in anion selectivity, we tested multiple substitutions and found bulky basic residues to be less effective than alanine in enhancing the relative permeability of large anions (Extended Data Fig. 6a–d). These studies underscore the importance of structure-based functional analyses.

In this study, we identify for the first time pore-lining residues of CaCC based on structural analyses of TMEM16A as well as mutagenesis of these highly conserved pore-lining residues (Extended Data Fig. 10). Unlike previous efforts searching among positively charged residues for those involved in anion permeation[12,25,28], we tested residues facing water-filled potential pore structures to delineate the permeation pathway based on the involvement of pore-lining residues in anion selectivity. For ion permeation and channel gating, we classify pore-lining residues into two groups: one group is distributed along the entire pore and is important for anion selectivity, and the other group is clustered together and is important for gating. For the first group, we validated the ability of ten pore-lining residues to interact with permeant ions by showing that mutations of these residues alter anion selectivity in this study and in two previous studies[25,28]. Visualization of the pore-lining residues and functional assessments of their role in anion selectivity thus firmly establishes their pore assignment. For the second group, we demonstrate a role for seven residues facing the constricted pore in channel gating, indicating that channel opening likely involves displacement of these residues that affect the relative stability of the open and closed states. Our study provides an essential framework to guide further studies of gating and anion permeation of calcium-activated chloride channels.

METHODS

Protein expression and purification

Truncated mouse TMEM16A was C-terminally fused to a 3C consensus sequence, a Strep-tag II peptide, and a GFP moiety and expressed in HEK293 GnTi^{-} cells using the BacMam system as described previously[29,30].

Protein purification and sample processing were carried out at 4°C. For nanodisc-reconstituted preparations, approximately 10 g of cell pellet (from about 1 L culture) was lysed by stirring for 40 min in 200 ml hypotonic buffer containing 50 mM $TrisNO_3$ (pH 9.0) supplemented with 0.1 mg/ml DNase, 1× complete protease inhibitor cocktail (Roche) and 1 mM phenylmethylsulfonyl (PMSF). The membrane fraction was collected by centrifugation at 30,000g for 30 min, and then homogenized with a Dounce homogenizer in extraction buffer containing 50 mM $TrisNO_3$ (pH 9.0), 150 mM KNO_3, and 10 mM $CaCl_2$ supplemented with 0.1 mg/ml DNase, 1× complete protease inhibitor cocktail, and 1 mM PMSF. Protein was extracted in 200 ml extraction buffer plus 0.5% n-dodecyl-b-d-maltopyranoside (DDM) and 0.1% cholesteryl hemisuccinate (CHS) with gentle stirring for 2 h. The insoluble fraction was removed by centrifugation at 30,000g for 30 min. The recombinant protein was affinity purified with an anti-GFP nanobody immobilized on CNBr-activated sepharose resin (GE Healthcare) in wash buffer containing 10 mM $TrisNO_3$ (pH 9.0), 150 mM KNO_3, 1 mM $CaCl_2$, 0.05% DDM, and 0.01% CHS supplemented with a 0.1 mg/ml lipid mixture containing 1-palmitoyl-2-oleoyl-sn-glycero-3-phosphocholine (POPC), 1-palmitoyl-2-oleoylsn-glycero-3-phosphoethanolamine (POPE) and 1-palmitoyl-2-oleoyl-sn-glycero-3-phospho-L-serine (POPS) at a ratio of 3:1:1. The purified protein was recovered by incubation with 1.5 CV wash buffer containing 0.5 mM dithiothreitol (DTT) and 50 mg 3C protease overnight. To reconstitute the protein in nanodiscs, the lipid was prepared as described previously in buffer containing 10 mM $TrisNO_3$ and 150 mM KNO_3. After purification, the protein sample was mixed with MSP2N2 and soy PC (Avanti) at a molar ratio of TMEM16A monomer: MSP2N2: soy PC = 1:4:100. The mixture was allowed to equilibrate for 1 h and Bio-beads SM2 (Bio-Rad) were added to the mixture three times within 24 h to gradually remove detergents from the system. Afterwards, the sample was filtered through a 0.45 μm filter, and reconstituted protein was separated on a Superdex-200 column in column buffer containing 10 mM $TrisNO_3$ (pH 9.0), 150 mM KNO_3, and 1 mM $CaCl_2$. The peak fraction was collected and concentrated to 0.6–0.7 mg/ml using a 100 kDa MWCO Amicon Ultra filter device (Millipore). The lipid compositions used for protein purification and nanodisc reconstitutions are chosen based on previous studies[30,31].

The same purification procedures were used to prepare LMNG solubilized preparations except 5 mM LMNG was in the extraction buffer and 0.02 mM LMNG was used in the wash buffer instead of DDM and CHS. After digestion by 3C, the protein was collected and immediately separated on a Superdex-200 column in column buffer containing 10 mM $TrisNO_3$ (pH 9.0), 150 mM KNO_3 and 1 mM $CaCl_2$. The peak fractions were collected and concentrated to 1 mg/ml using 100-kDa Amicon Ultra filter device.

N-[4-(7-diethylamino-4-methyl-3-coumarinyl)phenyl] maleimide (CPM) assay of TMEM16A stability as function of calcium concentration

To assess the stability of TMEM16A in the presence of a range of Ca^{2+} concentrations via CPM assay[16], we dialyzed TMEM16A in nanodiscs or LMNG in solutions containing buffered calcium made (at pH7.5 buffered with HEPES) by combining $Ca(OH)_2$ and EGTA to a ratio predicted by CaBuf softward (KU Leuven). Calcium concentrations of the solutions containing dialyzed TMEM16A protein preparations were subsequently measured

directly against calcium standards, using a Fluo-8 fluorescent assay in a BioTek Synergy H4 plate reader. MSP proteins have no cysteines and empty nanodiscs generate no CPM fluorescence signals[17], so the CPM signal measured via a fluoromax fluorometer (excitation at 387 nm, emission at 463 nm) provides a readout of cysteine exposure upon unfolding of TMEM16A at temperature ranging from 25°C to 75°C.

Isolation of monoclonal Fab (fragment antigen binding) for TMEM16A

To obtain Fabs to be used as fiducial markers for cryo-EM studies, TMEM16A was reconstituted into nanodiscs to provide a native-like lipid bilayer environment for presentation of the calcium-activated chloride channel to the recombinant Fab library. Once reconstituted, TMEM16A in nanodiscs was used for in-solution selections. A subtractive (nanodisc alone) and competitive panning strategy was used to find selective binders for TMEM16A, from our fully human naïve Fab phage library[18,19]. The selections yielded 23 clones with a signal 4 times higher than the background in an ELISA assay. Out of these 23 clones, 3 clones showed a very specific signal for TMEM16A and almost no signal for empty nanodiscs. Clone 2F11 was then expressed and purified, and complex formation with TMEM16A was tested with size exclusion chromatography. Fab(2F11) and TMEM16A indeed formed a complex which was also demonstrated by two-dimensional class averages of electron microscopy negative stain images (Extended Data Fig. 3b).

Electrophysiology

HEK293 cells were maintained at 37°C and 5% CO_2 in Dulbecco's Modified Eagle's Medium supplemented with 10% Fetal Bovine Serum and 1% penicillin/streptomycin, and were passaged upon reaching confluency (every 2–4 days) by digestion with 0.05% Trypsin-EDTA. 24 hours before recording, cells were transiently transfected with TMEM16A constructs using Lipofectamine 2000 (Invitrogen). On the morning before recording, cells were re-plated onto poly-L-lysine coated coverslips using trypsin and allowed to settle for at least 1 hour.

For patch clamp electrophysiology, coverslips were transferred into a recording bath solution containing 140 mM NaCl, 10 mM HEPES, and 5 mM EGTA, with pH adjusted to 7.2 with NaOH and osmolarity adjusted to 305–315 mOsm with mannitol. All recordings were made at room temperature. For whole cell recordings, intracellular solutions contained 140 mM NaCl, 10 mM HEPES, 1 mM $CaCl_2$ and 2 mM $MgCl_2$ with pH adjusted to 7.2 with NaOH and osmolarity adjusted to 310 mOsm with mannitol. For anion selectivity measurements, recordings from HEK293 cells transiently expressing wild-type or mutant TMEM16A under bi-ionic conditions using whole-cell patch-clamp and subjected to one-second ramp protocols between −80 and +80 mV. Extracellular solutions are exchanged between voltage ramp commands and contain 140 mM NaCl, 140 mM NaI, or 140 mM NaSCN. Permeability ratios for iodide/chloride ions (2.70 ± 0.09, N = 28 for WT; 3.73 ± 0.12, N = 11 for N542A; 5.32 ± 0.25, N = 9 for D550A; 4.85 ± 0.16, N = 7 for N587A; 4.00 ± 0.16, N = 9 for V595A; 1.82 ± 0.08, N = 7 for S635A; 4.65 ± 0.06, N = 5 for Q705A; 4.45 ± 0.10, N = 6 for F712A), or thiocyanate/chloride ions (5.47 ± 0.21, N = 28 for WT; 8.99 ± 0.24, N = 8 for N542A; 13.33 ± 0.66, N = 9 for D550A; 9.10 ± 0.29, N = 7 for N587A; 9.96 ± 0.30, N = 9 for V595A; 3.24 ± 0.26, N = 7 for S635A; 13.36 ± 0.32, N = 5 for Q705A;10.78 ± 0.34, N =

6 for F712A), are calculated by fitting the GHK equation to currents recorded using voltage ramps (Extended Data Fig. 6d). For Fig. 3d, the reversal potential (at 0 nA) is −46 mV for WT and −57 mV for N587A in external SCN^-, −27 mV for WT and −40 mV for N587A in external I^-, −2 mV for WT and 0 mV for N587A in external Cl^-.

For inside out patch recording, intracellular solutions consisted of normal bath solution supplemented with 2 mM $MgCl_2$. Intracellular solutions with varying calcium concentrations were generated by buffering calcium ions with EGTA at pH 7.2 and were made by combining $Ca(OH)_2$ and EGTA to a ratio predicted by CaBuf software (KU Leuven) and then adding 140 mM NaCl or NMDG-Cl and 10 mM HEPES to the desired volume. Calcium concentrations were subsequently measured directly against calcium standards using a Fluo-8 or Fluo-8FF fluorescent assay in a BioTek Synergy H4 plate reader. To assess calcium sensitivity of channel activation via recordings from inside-out patches excised from HEK293 cells transiently expressing wild-type or mutant TMEM16A, the membrane potential was held at +60 mV, and patches were exposed to intracellular solutions containing 140 mM NaCl and increasing concentrations of free Ca^{2+}. Solutions (**a**)–(**f**) in Fig. 4d contained 150 nM, 300 nM, 400 nM, 600 nM, 5.5 μM, and 1 mM free Ca^{2+}, respectively. Ca^{2+}-dependent currents from wild-type (WT) and mutant TMEM16A channels were normalized to their maximum values and fit to the Hill equation. The EC_{50} values in nM (796 ± 66, N = 10 for WT; 295 ± 24, N = 10 for N542A; 148 ± 31, N = 6 for I546A; 192 ± 13, N = 6 for Y589A; 252 ± 17, N = 6 for I592A; 2036 ± 52, N = 7 for V595A; 2008 ± 63, N = 7 for L639A; 205 ± 30, N = 8 for F708A) were compared using one-way ANOVA followed by the Bonferroni post-hoc test for significance (Extended Data Fig. 9c).

External or internal solutions using alternate anions were made by replacing NaCl with the indicated sodium salt at equimolar concentrations. Patch pipettes were pulled from 1.5/0.86 (OD/ID) glass and polished to 2–2.5 MΩ resistance (inside-out patch) or 3–5 MΩ (whole cell patch). Perfusion exchange was performed using a VM-8 perfusion apparatus with Octaflow software (ALA Scientific). Data were collected at 10 kHz sampling rate and low pass filtered online at 1 kHz. Recordings were made using an Axon Instruments Multiclamp 700 with Digidata 1440 and were collected into pClamp10 software. All patch clamp seals were allowed to reach at least 3 GΩ resistance before patch rupture, but typical seal resistance usually exceeded 10 GΩ. All recordings were made using a 1 M KCl agar bridge to prevent baseline fluctuation at the reference electrode.

For Data analysis, all offline data analysis for patch clamp recording was performed using Graphpad Prism 6, Clampfit 10, and Microsoft Excel. Permeability ratios were determined from bi-ionic conditions using a reduced form of the Goldman-Hodgkin-Katz voltage equation:

$$E_{\mathrm{REV}} = \frac{RT}{zF}\mathrm{Ln}\frac{P_{\mathrm{X}}[\mathrm{X}^-]_o}{P_{\mathrm{Cl}}[\mathrm{Cl}^-]_i}$$

where P_X represents relative permeability of ion species "X" and F, R and T have their usual thermodynamic meanings. Concentration-dependence curves for Ca^{2+} were generated by fitting data to an equation of the form:

$$\frac{I}{I_{\mathrm{MAX}}} = \frac{1}{1+\left(\frac{K_D}{[\mathrm{Ca}^{2+}]}\right)^{n_H}}$$

Where I/I_{MAX} denotes current normalized to the maximum amplitude in the highest $[Ca^{2+}]$ tested, K_D denotes the dissociation constant for that ion and n_H denotes the Hill coefficient. Statistical analysis for data acquired using patch clamp employed one-way ANOVA followed by Bonferroni post-hoc tests for statistical significance. $p < 0.01$ was used as a threshold for significance.

Electron microscopy

For negative staining, 2.5 μl of purified TMEM16A at a concentration of 0.02 mg/ml were placed on home-made continuous carbon grids glow discharged for 30 sec and coated with 0.75% (w/v) uranyl formate for 30 sec. Grids were imaged on a Tecnai T12 microscope (FEI Company) operated at 120 kV with a 4k×4k scintillator-based charge-coupled device camera UltraScan 4000, (Gatan). A nominal magnification of × 52,000, corresponding to a pixel size of 2.21 Å on the specimen, and a defocus around −1.5 μm were used for image recording.

For cryo-EM, 2.5 μl of purified TMEM16A at a concentration of approximately 0.5 mg/ml were applied to holey carbon grids (Quantifoil 400 mesh Cu R1.2/1.3) glow-discharged for 30 sec. After 30 sec incubation on the grids at 4°C under 100% humidity, grids were blotted with Whatman #4 filter paper for 6–8 sec and plunge-frozen in liquid ethane cooled by liquid nitrogen using a FEI Mark III Vitrobot. Grids were transferred to an FEI Titan Krios electron microscope equipped with a field emission electron source and operated at 300 kV at the Howard Hughes Medical Institute Cryo-EM facility at Janelia Research Campus.

Images were recorded using SerialEM[32] in super-resolution mode using a Gatan K2 Summit direct electron detector (Gatan) at a calibrated magnification of 29,000X, yielding a physical pixel size of 1.02 Å (0.51 Å super resolution pixel size). A dose rate of 10 electrons per physical pixel per second and an exposure of 8 sec were used for data collection with 0.2 sec subframes to give a total dose of 80 electrons per $Å^2$.

Data processing

For negative-stain data, Simplified Application Managing Utilities for EM Labs (SAMUEL) scripts[33] were used for particle picking and 2D classification. In this package, 2D classification was carried out by ten cycles of correspondence analysis, *k*-means classification, and multi-reference alignment using SPIDER operations 'CA S', 'CL KM,' and 'AP SH'[34].

For Cryo-EM data, drift correction was performed using MotionCor2[35] and images were binned 2×2 by Fourier cropping to a pixel size of 1.02 Å. The contrast transfer function

(CTF) was estimated using CTFFIND4[36] (LMNG) or GCTF[37] (Nanodisc) using motion-corrected sums without dose-weighting. Motion-corrected sums with dose-weighting were used for all other image processing. RELION (1.4 and 2.1beta1, in which the bug on gold standard refinement procedure was fixed)[38] was used for 2D classification, 3D classification, and refinement procedures.

For the LMNG dataset, around 4000 particles were manually picked and classified by 2D classification in SAMUEL to generate the templates for automatic particle picking with samautopick.py. 533,545 particles were identified after manually inspection of auto-picked particles. These particles were subjected to 2D classification, using RELION 1.4. A total of 342,875 particles from 2D classes that show clear structural features were combined and binned 4 to a pixel size of 4.08 Å for 3D classification. The crystal structure of nhTMEM16A (PDB:4WIS) was converted to a density map with e2pdb2mrc.py[39] and low pass filtered to 60 Å as the initial model for 3D classification and refinement using RELION 1.4 without applied symmetry. After 3D classification, images without binning with a pixel size of 1.02 Å were used for further auto-refinement with a C2 symmetry. Two of five classes, which gave maps with resolution better than 5 Å (4.6 Å and 4.9 Å), were combined together for another round of 3D refinement to generate a 4.0 Å map. The resolution was further improved to 3.8 Å by adding particles from other three classes.

The TMEM16A with Fab bound dataset was processed with the same strategy as for TMEM16A in LMNG. Starting with 338,705 particles from automatic particle picking and 2D classification by RELION, 132,444 particles from 4 classes that present clear side views were combined together for 3D auto-refinement. Then the Fab density for each particle was subtracted with script projection_subtraction.py (written by Danniel Arsanow in Cheng lab at UCSF) based on final data.star file containing Eular angle information from 3D refinement. The 132,444 subtracted particles without Fab density were combined with the 342,875 particles from all five 3D classes of TMEM16A in LMNG dataset and processed for 3D auto-refinement. After refinement have converged, the final data set was subjected to ‘post-processing’ in RELION, in which a soft mask was calculated and applied to the two half-maps before calculating the corrected FSC and the resolution was estimated using FSC=0.143 criterion[40] on the corrected FSC curves in Fourier space in which the influences of the mask were removed. During this step, temperature-factor estimation and map sharpening were also performed to get final map at resolution of 3.4 Å.

For the Nanodisc dataset, particle picking performed with the Gautomatch program (developed by Dr. Kai Zhang, MRC Laboratory of Molecular Biology, Cambridge, UK, http://www.mrc-lmb.cam.ac.uk/kzhang/Gautomatch/) with templates from 2D classes of the LMNG dataset generated 927,414 particles in total. All particles were extracted and binned 4 (pixel size 4.08 Å) and 2D classified using RELION. 341,875 particles selected from good 2D classes were un-binned with a pixel size of 1.02 Å, and were used for 3D refinement using an initial model low pass filtered from the LMNG structure that had been low pass filtered to a resolution of 60 Å, giving rise to a 5.5 Å map. This 5.5 Å map was low pass filtered to 10 Å as the initial model to apply for 3D classification without applied symmetry for all particles with pixel size of 4.08 Å. Two of seven classes gave a map with improved resolution (4.7 Å and 5.1 Å respectively) after 3D auto-refinement with C2 symmetry. These

two classes were combined and another 3D auto-refinement was run to generate the map at a resolution of 4.6 Å. Similar to LMNG dataset, the 'post-processing' in RELION was applied to the final data set and the final map was generated at resolution of 3.8 Å and used for model building.

Directional FSC is calculated using home-made script (see below). Local resolution estimates were calculated with unsharpened raw density maps using ResMap[41].

Model building

Ab initio model building was carried out in COOT[42] for all transmembrane helices and small parts of soluble domains. Initial placement of TM helices was made based on sequence alignment with the nhTMEM16A (PDB accession 4WIS)[10]. For major part of soluble domain, the resolutions are insufficient for assignments. For these parts, we used homology model that was generated with swiss-model based on a sequence alignment with the crystal structure of nhTMEM16A[10], and refined against the EM map on MDFF[43]. For the transmembrane region, the model was refined both in real space with Phenix.real_space_refine[44] and also in Fourier space with REFMAC[45], followed by further manual adjustment in COOT. This process was repeated until Ramachandran validation was satisfied. Side chain assignments were further validated by using difference densities calculated by subtracting a simulated map based on the Ca only model from the experimental map. The model building following similar procedure was carried out independently by four individuals and cross-validated to ensure the accuracy of assignments. Additional validation of the final model was carried out using MolProbity[46] and EMRinger[47].

For cross-validation, the final model was refined against one of the half maps generated in RELION. FSC curves were then calculated between the refined model and half map 1 ('work,' used in test refinement), the refined model and half map 2 ('free,' not used in test refinement), and the refined model and the summed map. There is no notable gap between 'work' and 'free' FSC curves, indicating little effect of over-fitting. In this process, the final model was displaced and then refined against the half-map (work). Then this model was used for calculation of cross-validation. Using FSC = 0.5 criterion, the resolution estimated from cross-validation is about 4.5 Å for nanodisc-reconstituted TMEM16A and 3.8 Å for LMNG-solubilized TMEM16A.

HOLE[20] was used to calculate the pore profile shown in Fig. 3 and Fig. 4. The narrowest point is defined as the location of the pore with the smallest radius. For those pore-lining residues that are not completely resolved, a solid line and a dotted line are drawn based on positioning two rotamers that will provide the largest and smallest estimate for the pore radius at that location. The program PyMol[48] was used to calculate surface representation of electrostatic potentials.

Difference map calculation

We used "omit density" to assign the position of one or two Ca^{2+} ions. It was calculated by subtracting a map calculated based on the refined atomic model without any ligand from the experimental density map, i.e. density – model. In this difference map, any experimental

map features not included in the atomic model, such as densities contributed by bound ions, appear as positive densities. The map was calculated using PHENIX[44] with the command line option “phenix.real_space_diff_map” available in the 2017-07-07 nightly build: first a theoretical map was calculated from LMNG and nanodisc structures at a resolution of 4 Å and 3.8 Å resolution, respectively, corresponding to the resolution at which the model refinement was performed. The electron scattering factors were used. Then the calculated map was subtracted from the respective experimental electron density maps. The difference maps clearly show the presence of one Ca^{2+} ion in the LMNG structure and two in the nanodisc one. Ca^{2+} ion positions were assigned based on the residual density between the actual experimental data and the density calculated from the model and, with a threshold of $\sigma = 7$ and $\sigma = 10$ for densities corresponding to nanodisc and LMNG respectively (Fig. 2h).

Calculation of directional Fourier shell correlation (dFSC)

The Fourier shell correlation (FSC) between two half-maps was calculated as described previously[49,50], except conical shells were used instead of spherical shells to allow calculation of the FSC in different directions. Cones with an apex angle of 20° were sampled on a 500-point Fibonacci spherical grid where the apex of a particular cone is at the center of the sphere and the central axis of that cone lay on the vector joining the center of the sphere with a grid point on the surface of the sphere. This analysis resulted in 500 1D directional FSC (dFSC) curves, which were averaged to generate a global average dFSC curve. A 3D representation of the dFSC analysis was generated by constructing a sphere from the cones oriented in their respective directions and setting each conical shell of each cone to its respective dFSC value. dFSC values were averaged in regions of overlap between cones and a 3 pixel × 3 pixel × 3 pixel median filter was applied three times to the 3D dFSC map in *UCSF Chimera*[51] to reduce noise. The resolution in different directions was determined as the spatial frequency with a dFSC value of 0.143, the same criterion as generally used for the FSC[52]. The trend in anisotropy of resolution that is observed at FSC = 0.143 is also observed at other FSC thresholds irrespective of the shape of the cones used in dFSC calculations.

Extended Data

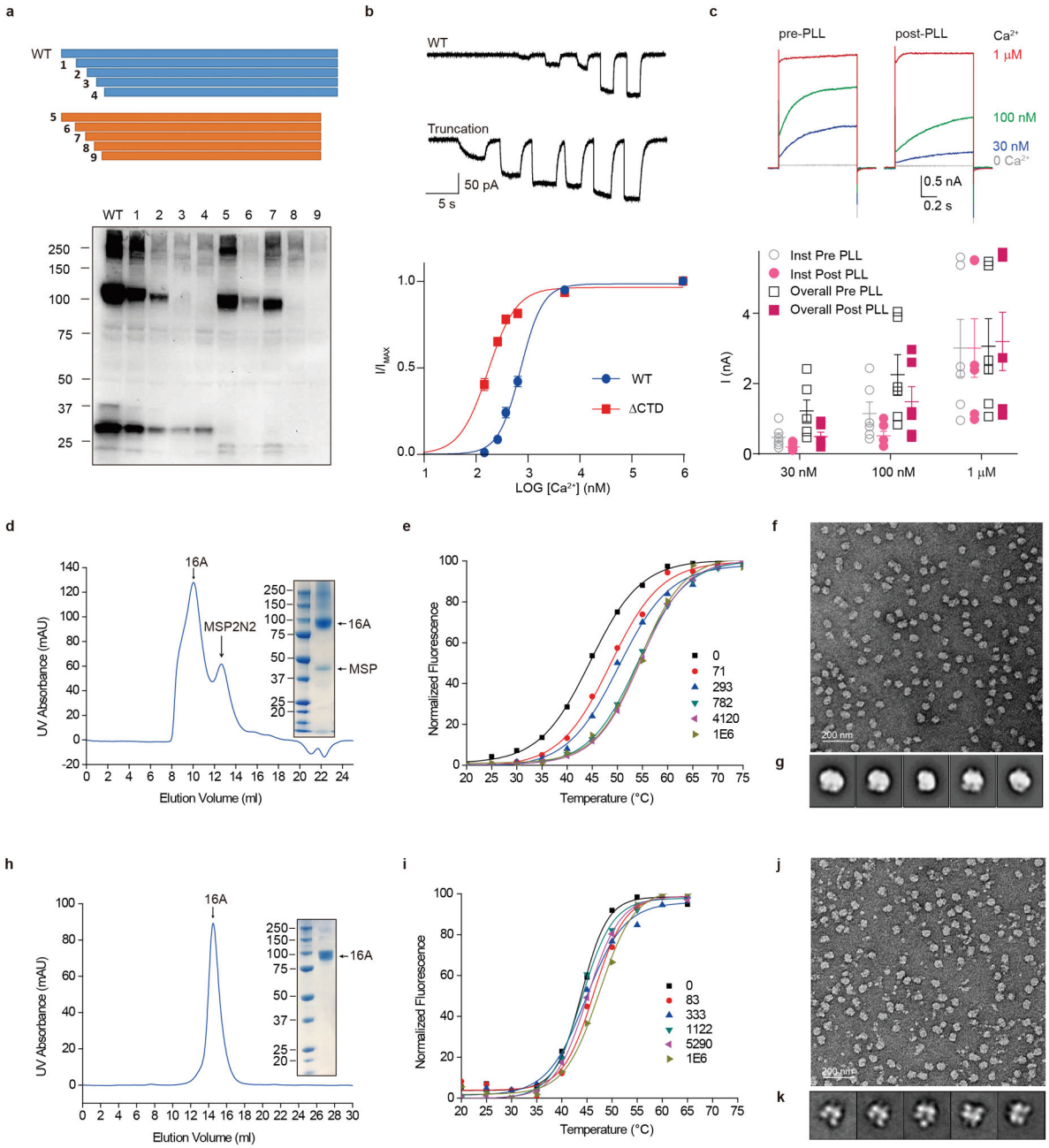

Extended Data Figure 1. TMEM16A protein purification and negative staining

a, Western blot (bottom) of nine TMEM16A constructs with different N-terminal and/or C-terminal truncations (diagramed, top). Construct 5 corresponding to mouse TMEM16A residues 1–903 was selected for this study for the absence of the smaller fragment of ~30 kD on the western blot as well as its high expression. **b,** Top, representative trace of inside-out patch from HEK293 cells transiently transfected with wild-type TMEM16A (WT) or Construct 5. The membrane potential was held at +60 mV, and patches were exposed to

intracellular solutions containing 140 mM NaCl and 150 nM, 300 nM, 400 nM, 600 nM, 1.8 μM, or 1 mM free Ca^{2+}. Repeated independently four times with similar results. Bottom, normalized chloride currents were fit to the Hill equation. EC_{50} for Ca^{2+} sensitivity is 178 ± 14 nM for construct 5 (four independent experiments) and 796 ± 66 nM for WT (ten independent experiments; $p < 0.0001$, see Extended Data Fig. 9c). **c**, Top, poly-L-lysine (PLL, 30 μg/mL) treatment for 30 sec to reduce PIP_2 and other lipids with negatively charged head groups caused desensitization of TMEM16A with C-terminal truncation (a.a. 1–903) in excised inside-out patch exposed to 150 mM NaCl on both sides of the membrane, as evident from the reduction of Ca^{2+} sensitivity. Repeated independently six times with similar results. Bottom, following the PLL treatment the current amplitudes were reduced at 30 nM Ca^{2+} and 100 nM Ca^{2+} ("Inst" for the "instantaneous" current amplitude at the start of depolarization from a holding potential of 0 mV to +100 mV, $p = 0.02$ from two-way ANOVA between "Pre" and "post" PLL; "Overall" for the current amplitude at the end of depolarization, $p = 0.004$ from two-way ANOVA between "Pre" and "Post"; 6 independent experiments) but not at 1 μM Ca^{2+} (Sidak's multiple comparisons, $p > 0.99$ and $p = 0.73$ for "Inst" and "Overall", respectively). Mean ± SEM are shown in **b** and **c. d**, Size-exclusion chromatography of TMEM16A reconstituted into lipid nanodiscs with MSP2N2. The peak fractions corresponding to nanodisc-reconstituted TMEM16A (16A) and free MSP2N2 are indicated. The 16A peak fraction was examined by SDS-polyacrylamide gel electrophoresis (SDS-PAGE). TMEM16A and MSP2N2 (MSP) monomers are approximately 105 kDa and 46 kDa, respectively. The faint band at 210 kDa may correspond to incompletely disassociated TMEM16A dimers. **e**, CPM analysis[16,17] of nanodisc-reconstituted TMEM16A in 0, 71 nM, 293 nM, 782 nM, 4120 nM or 1 mM Ca^{2+}. **f,** Raw micrographs of nanodisc-reconstituted TMEM16A examined by negative-stain EM. **g,** 2D class averages of particles from negative-stain EM of TMEM16A reconstituted into nanodiscs **h,** Size-exclusion chromatography of TMEM16A solubilized in LMNG. The peak fraction was examined by SDS-PAGE. **i**, CPM analysis of LMNG-solubilized TMEM16A in 0, 83 nM, 333 nM, 1122 nM, 5290 nM or 1 mM Ca^{2+}. **j,** Raw micrographs of LMNG-solubilized TMEM16A examined by negative-stain EM. Both micrographs, (f) and (j), showed mono-dispersed and homogeneous particles. **k,** 2D class averages of particles from negative-stain EM of TMEM16A solubilized in LMNG.

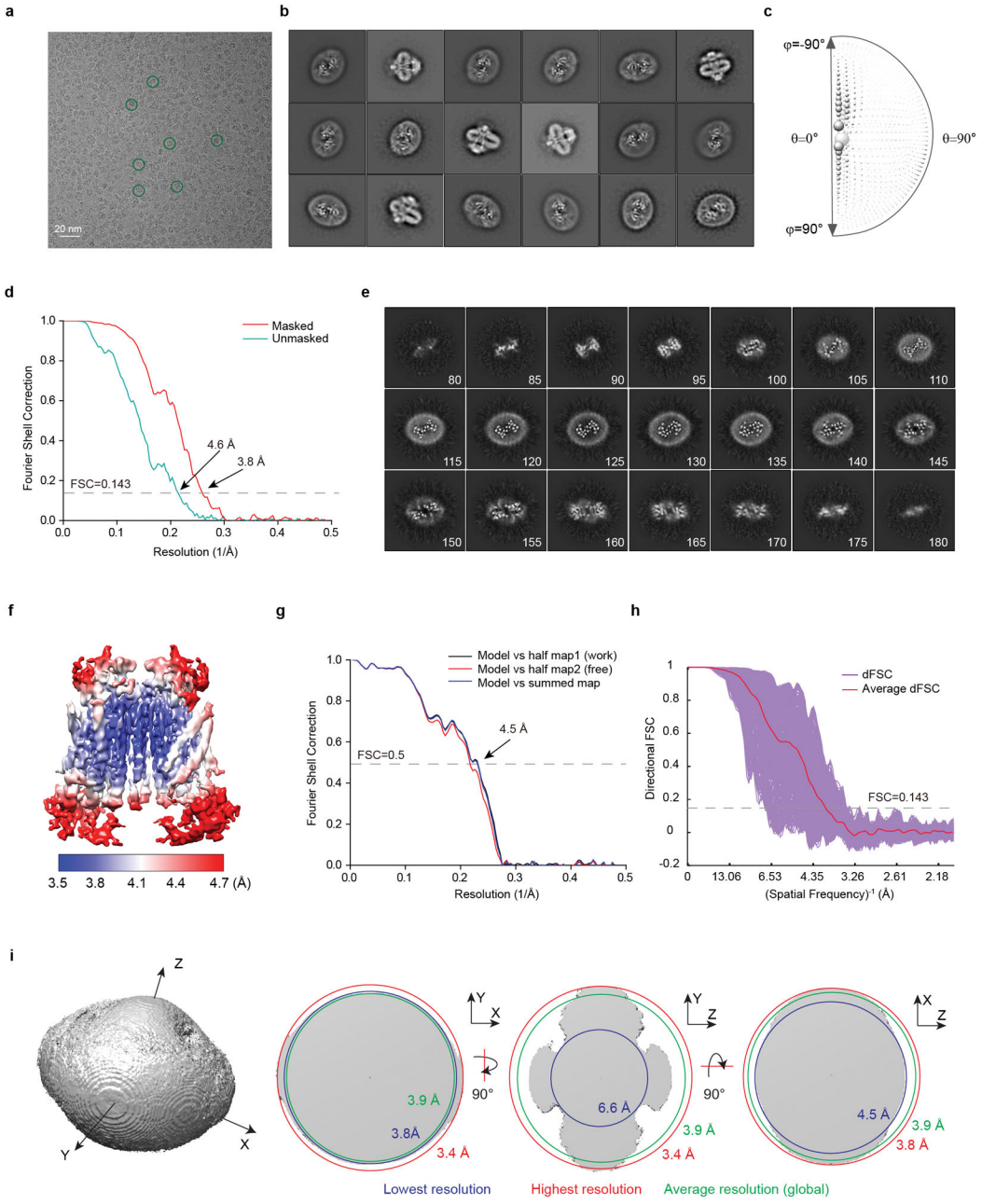

Extended Data Figure 2. Cryo-EM analysis of TMEM16A reconstituted in nanodiscs

a, A representative cryo-EM micrograph of nanodisc-reconstituted TMEM16A. Green circles indicate individual particles. **b**, Representative 2D class averages from boxed particles with 256-pixel box size (261.12 Å). **c**, Eular angle distribution of all particles included in the final 3D reconstruction. The size of the spheres is proportional to the number of particles seen from that specific orientation. **d**, FSC curves of two independently refined maps before (blue) and after (red) post-processing in RELION. Curves with resolution corresponding to FSC = 0.143 are shown. **e**, Planar slices through the unsharpened EM density map at different levels along the channel symmetry axis. **f,** Local resolution of

TMEM16A as estimated by RELION and shown with pseudo-color representation of resolution. **g**, Cross-validation using FSC curves of the density map calculated from the refined model versus half map 1 (work), versus half map 2 (free), and versus summed map. **h**, Directional FSC from different Fourier cones. Each curve indicates a different direction. **i**, Calculated resolution from different views. The directions are indicated as *x*, *y*, and *z* in the 3D resolution map. The highest and lowest resolutions are labeled with red and blue circles respectively. The green circle shows global average resolution.

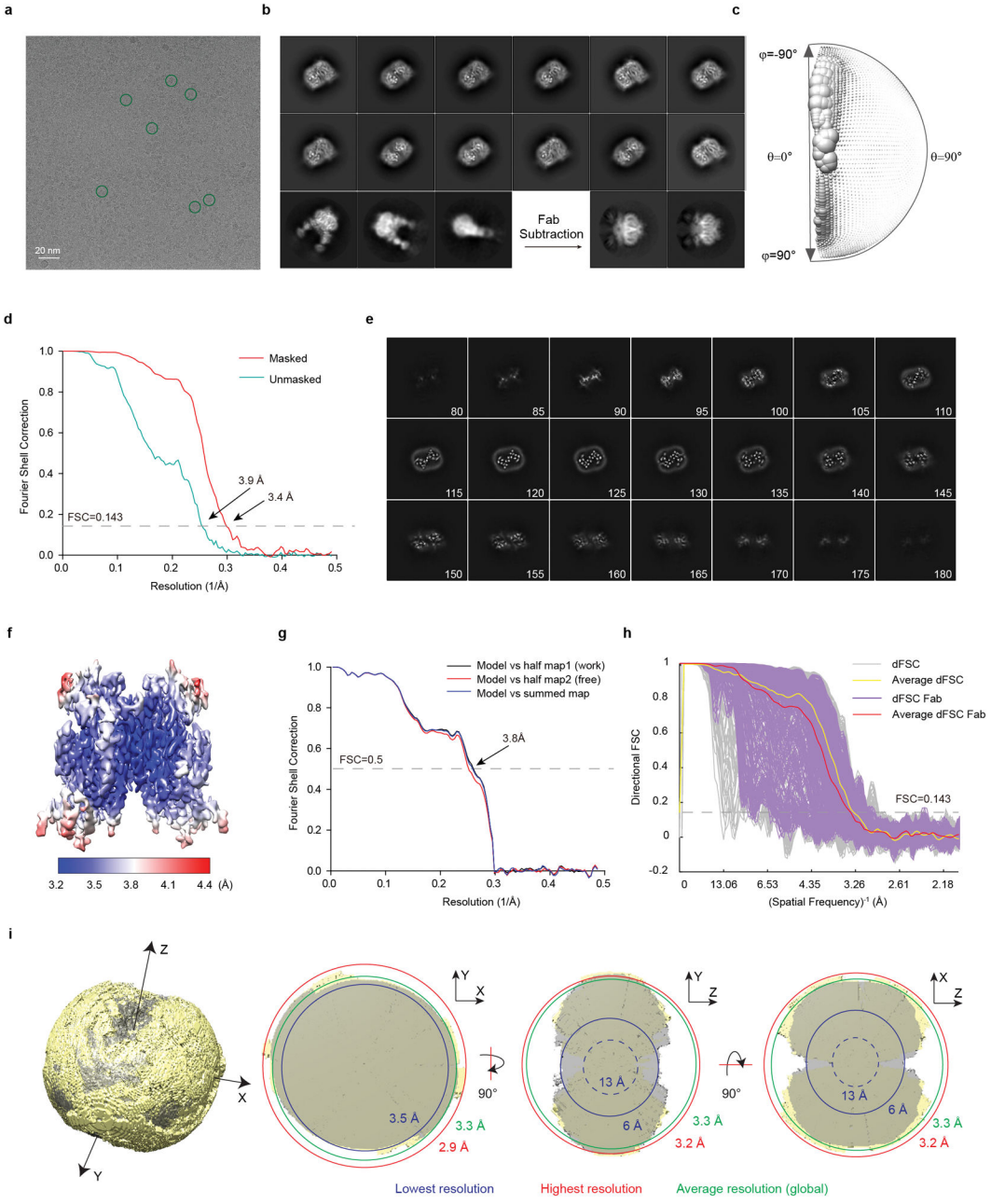

Extended Data Figure 3. Cryo-EM analysis of TMEM16A solubilized in LMNG

a, A representative cryo-EM micrograph of LMNG-solubilized TMEM16A. Green circles indicate individual particles. **b**, Representative 2D class averages from boxed particles with a 256 pixels box size (261.12 Å) and TMEM16A in complex with Fabs (bottom row, with the two right panels showing particles after subtraction of densities for Fabs). **c**, Eular angle distribution of all particles included in the final 3D reconstruction. The size of the spheres is proportional to the number of particles visualized from that specific orientation. **d**, FSC curves of two independently refined maps before (blue) and after (red) post-processing in RELION. Curves with resolution corresponding to FSC = 0.143 are shown. **e**, Planar slices through the unsharpened EM density map at different levels along the channel symmetry axis. **f**, Local resolution of TMEM16A as estimated by RELION and shown with pseudo-color representation of resolution. **g**, Cross-validation using FSC curves of the density map calculated from the refined model versus half map 1 (work), versus half map 2 (free), and versus summed map. **h**, Directional FSC (dFSC) from different Fourier cones. Each curve indicates a different direction. dFSC for TMEM16A alone in LMNG in grey (average in yellow); dFSC for combination of TMEM16A alone and with Fabs bound in LMNG in purple (average in red). **i**, Calculated resolution from different views (grey for combination of TMEM16A alone and with Fabs bound, yellow for TMEM16A alone). The directions are indicated as *x*, *y*, and *z* in the 3D resolution map. The highest and lowest resolutions are labeled with red and blue circles respectively. The green circle shows global average resolution.

a

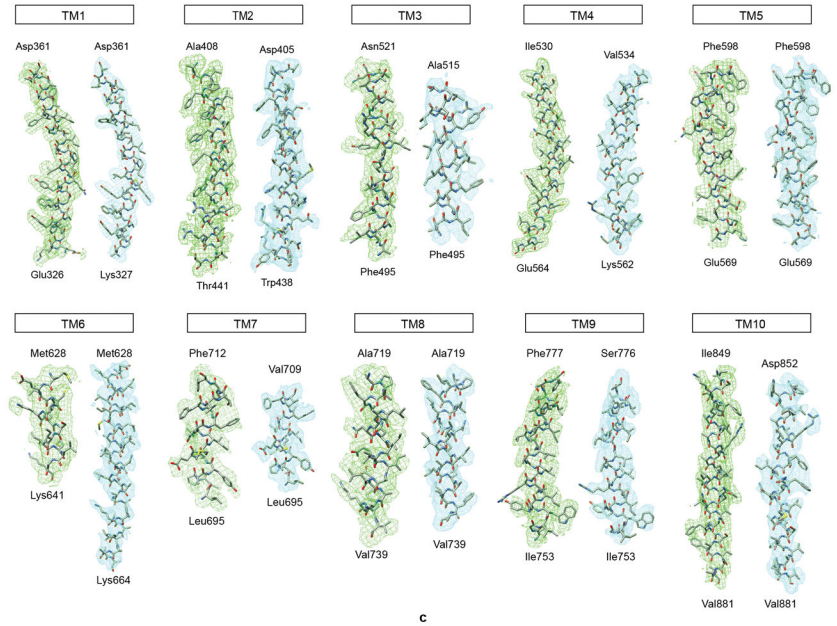

b

Summary of Cryo-EM Data Collection and Model Refinement

	Nanodisc	LMNG
Data Collection/Processing		
Voltage (kV)	300	300
Magnification	29,000	29,000
Defocus Range (μm)	-0.9 – -2.2	-0.8 – -1.9
Pixel Size (Å)	1.02	1.02
Total Electron Dose ($e^-/Å^2$)	80	80
Exposure Time (s)	8	8
Number of Images	3149	5014
Number of Frames/Image	40	40
Initial Particle Number	927,414 (autopick)	533,545 (manual screen)
Final Particle Number	251,851	342,875 (+132,444)*
Resolution (unmasked, Å)	4.6	3.78 (3.9)*
Resolution (masked, Å)	3.8	3.31 (3.4)*
Refinement		
Number of Atoms	8607	7592
RMS Deviations		
Bond Lengths (Å)	0.006	0.008
Bond Angles (°)	1.090	1.211
Ramachandran		
Favored (%)	93.7	90.87
Allowed (%)	6.1	8.92
Outlier (%)	0.2	0.21
Molprobity Score	1.72	2.38
EMRinger Score	2.22	1.13

*Combined dataset with Fab-subtracted information are show in parentheses.

c

Sidechain Assignment of TMEM16A in Nanodiscs

TMs	Residues within the TM Segment	Total Number of Residues	Number of Residues without Sidechain	Residues without Sidechain Assignment	Percentage with Sidechain Assignment
1	326-362	37	3	326,327,361	91.9%
2	407-438	32	3	409,425,429	90.7%
3	494-515	22	5	494,495,496,499,500	77.3%
4	528-568	41	6	533, 537, 541 550,551,564	85.4%
5	569-597	29	4	569,570,573,574	86.2%
6	625-664	40	18	628,633,635,641,649-651, 653,656-664	56.1%
7	691-718	28	2	692,698	92.9%
8	719-739	21	2	732, 736	90.5%
9	751-778	28	3	752,765,776	89.3%
10	850-883	34	4	852,873,876,879	88.2%
1-10		312	50	(residues listed above)	84.0%

d

Sidechain Assignment of TMEM16A in LMNG

TMs	Residues within the TM Segment	Total Number of Residues	Number of Residues without Sidechain	Residues without Sidechain Assignment	Percentage with Sidechain Assignment
1	326-361	36	8	326,327,340,341,352,354 359,361	77.8%
2	407-438	32	14	409,416,418,425,426,428,429, 430,431,432,434,435,436,438	56.3%
3	493-521	29	9	493,494,495,496,499,500,504, 518,520	67.0%
4	530-564	35	12	530,531,532,534,537,550,551, 558,559,562,563,564	65.7%
5	569-600	32	5	569,573,575,579,584	84.4%
6	628-647	20	2	628,647	90.0%
7	692-715	23	1	698	95.7%
8	716-740	25	1	732	96.0%
9	753-776	24	1	765	95.8%
10	852-875	24	1	872	95.8%
1-10		280	52	(residues listed above)	81.4%

Extended Data Figure 4. Cryo-EM densities of the ten transmembrane helices of TMEM16A, summary of cryo-EM data collection and processing, and summaries of sidechain assignments

a, Representative cryo-EM densities of the ten transmembrane helices (TM1-TM10) of nanodisc-reconstituted TMEM16A (right) or LMNG-solubilized TMEM16A (left) are superimposed on the corresponding atomic model. The EM densities are shown in blue meshes for nanodisc-reconstituted TMEM16A, or green meshes for LMNG-solubilized TMEM16A, and the model is show as sticks and colored according to atom type (C: light grey; N: blue; O: red; S: yellow). **b**, Summary of cryo-EM data collection and model

refinement. **c**, Summary of sidechain assignment of TMEM16A in nanodiscs. **d**, Summary of sidechain assignment of TMEM16A in LMNG.

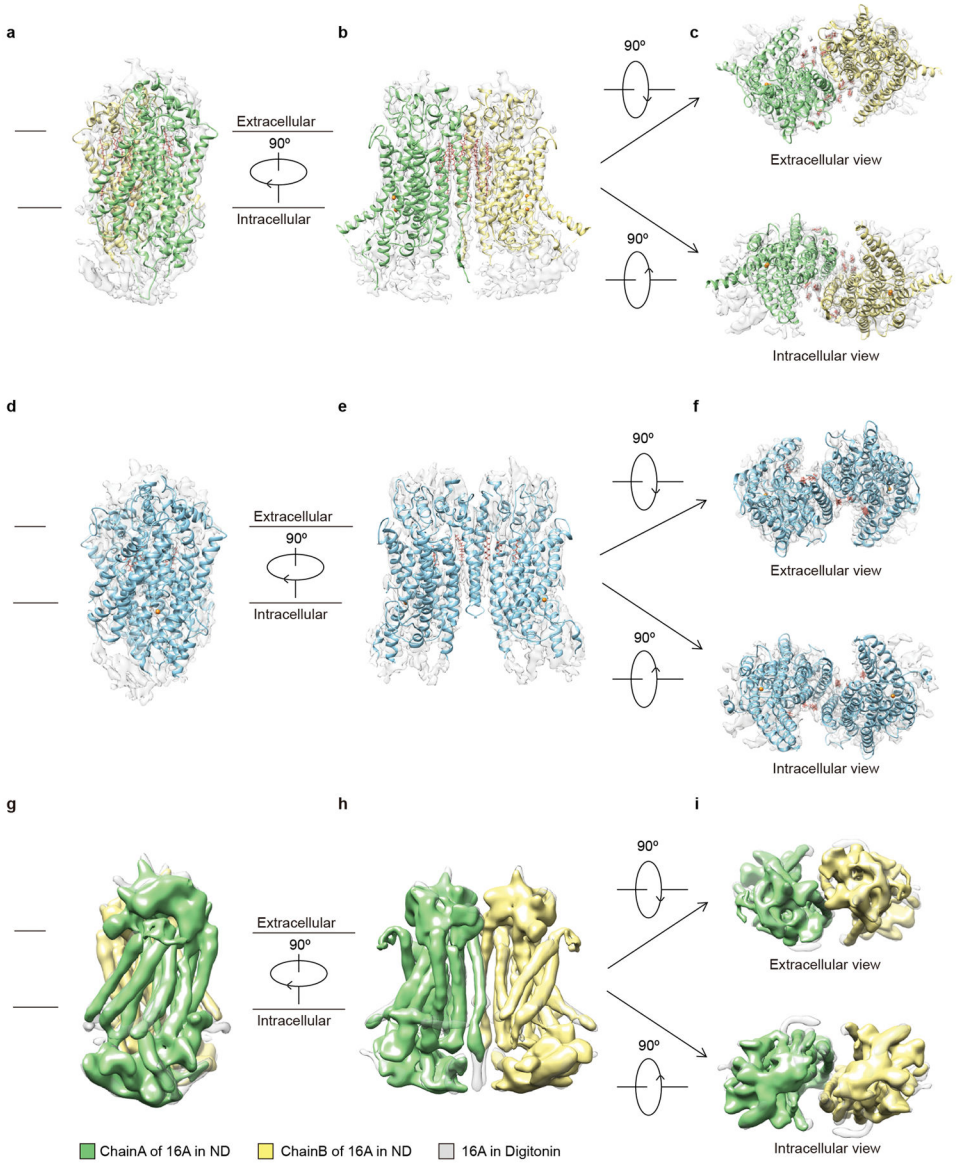

Extended Data Figure 5. Atomic models of TMEM16A in two conformations

a–c, Ribbon diagrams of TMEM16A reconstituted in nanodiscs (in green and yellow) with lipids (in red), overlayed with EM density map (sharpened, in light grey). Two Ca^{2+} ions (orange spheres) are present in each monomer. **d–f,** Ribbon diagrams of TMEM16A solubilized in LMNG (in blue) with lipids (in red), overlayed with EM density map (sharpened, in light grey). One Ca^{2+} ion (orange sphere) is present in each monomer **g–i,** EM densities of nanodisc-reconstituted TMEM16A (unsharpened, in green and yellow) overlayed with digitonin-solubilized TMEM16A[12] (in grey).

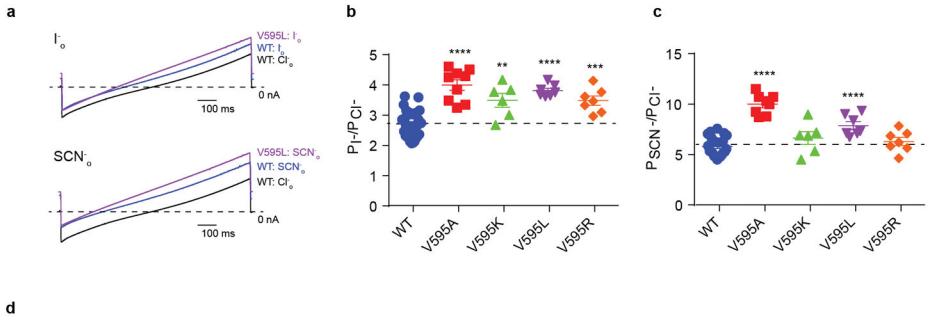

d

	Construct	P_I/P_{Cl} ± S.E.M.	N	P-value	P_{SCN}/P_{Cl} ± S.E.M.	N	P-value
	WT	2.70 ± 0.09	28	-	5.47 ± 0.21	28	-
TM3	S513A	2.64 ± 0.10	6	0.9996	4.55 ± 0.22	6	0.7299
	T514A	3.22 ± 0.16	5	0.2208	5.62 ± 0.40	5	0.9997
TM4	T533A	3.18 ± 0.10	5	0.3157	5.34 ± 0.15	5	0.9997
	T535A	3.02 ± 0.13	5	0.8936	4.92 ± 0.21	5	0.9943
	T537A	2.57 ± 0.13	5	0.9991	4.55 ± 0.21	5	0.8315
	N542A	3.73 ± 0.12	11	< 0.0001	8.99 ± 0.24	8	< 0.0001
	N542D	3.27 ± 0.16	7	0.0442	6.99 ± 0.45	7	0.0502
	L543A	2.82 ± 0.05	6	0.9992	4.40 ± 0.23	6	0.4941
	I546A	3.42 ± 0.12	6	0.0066	5.02 ± 0.14	6	0.9987
	I547A	2.53 ± 0.10	5	0.9988	4.16 ± 0.15	5	0.2991
	D550A	5.32 ± 0.25	9	< 0.0001	13.33 ± 0.66	9	< 0.0001
	E551A	2.64 ± 0.07	6	0.9996	5.55 ± 0.26	6	0.9998
TM4 -5 Linker	E569A	2.49 ± 0.18	5	0.9983	4.94 ± 0.45	5	0.9985
	E573A	2.90 ± 0.18	6	0.9983	6.14 ± 0.45	6	0.9823
TM5	N587A	4.85 ± 0.16	7	< 0.0001	9.10 ± 0.29	7	< 0.0001
	S588A	2.76 ± 0.16	8	0.9996	5.99 ± 0.56	8	0.9981
	P591A	2.87 ± 0.15	10	0.9983	5.66 ± 0.44	10	0.9994
	I592A	2.63 ± 0.13	6	0.9996	3.77 ± 0.23	6	0.0292
	V595A	4.00 ± 0.16	9	< 0.0001	9.96 ± 0.30	9	< 0.0001
	V595K	3.49 ± 0.21	6	0.0015	6.64 ± 0.58	6	0.3672
	V595L	3.81 ± 0.07	7	< 0.0001	7.86 ± 0.37	7	< 0.0001
	V595R	3.48 ± 0.14	7	0.0007	6.30 ± 0.37	7	0.7936
TM6	C631A	2.26 ± 0.16	6	0.3179	3.48 ± 0.24	6	0.0048
	S635A	1.82 ± 0.08	7	< 0.0001	3.24 ± 0.26	7	0.0003
	I637A	2.96 ± 0.13	7	0.9455	5.80 ± 0.23	6	0.9991
	L639A	2.28 ± 0.04	6	0.3804	3.86 ± 0.18	6	0.0486
	Q642A	2.64 ± 0.10	7	0.9996	3.95 ± 0.10	7	0.0010
TM6 -7 Linker	T696A	2.81 ± 0.16	6	0.9993	5.86 ± 0.57	6	0.9990
	P697A	2.74 ± 0.31	7	0.9997	5.68 ± 0.64	7	0.9994
TM7	Q705A	4.65 ± 0.06	5	< 0.0001	13.36 ± 0.32	5	< 0.0001
	F708A	3.20 ± 0.06	6	0.2212	7.87 ± 0.22	6	0.0002
	F712A	4.45 ± 0.10	6	< 0.0001	10.78 ± 0.34	6	< 0.0001
TM9-10 Linker	D780A	3.84 ± 0.14	7	< 0.0001	9.85 ± 0.50	7	< 0.0001
	Y787A	4.80 ± 0.15	5	< 0.0001	14.15 ± 0.82	5	< 0.0001
	Y789A	3.07 ± 0.13	6	0.6096	6.60 ± 0.48	7	0.3030
	Y791A	3.30 ± 0.07	7	0.0274	6.98 ± 0.16	7	0.0509
	N794A	2.89 ± 0.17	7	0.9983	5.40 ± 0.46	7	0.9998
	T796A	2.97 ± 0.11	9	0.8442	5.93 ± 0.55	9	0.9983
	H798A	3.14 ± 0.12	5	0.4512	5.71 ± 0.31	5	0.9994
	N802A	3.24 ± 0.19	7	0.0681	6.69 ± 0.35	7	0.2242
	H803A	3.77 ± 0.13	9	< 0.0001	7.53 ± 0.45	9	0.0002
TM10	W854A	3.22 ± 0.29	7	0.1219	5.11 ± 0.46	7	0.9990
	R860A	2.69 ± 0.38	6	0.9999	4.59 ± 0.37	6	0.8029
	F867A	3.33 ± 0.18	8	0.0133	5.83 ± 0.26	7	0.9990
	Q868E	2.91 ± 0.14	7	0.9980	5.12 ± 0.33	7	0.9990

Extended Data Figure 6. Anion selectivity depends on residues lining the pore surrounded by TM3–8 but not TM10 residues at the dimer interface

a, Bi-ionic conditions for assessing the effect of the V595L mutation on permeability ratios. **b,** Effects of different substitutions of V595 on the permeability ratio P_{I^-}/P_{Cl^-} (2.70 ± 0.09, N = 28 for WT; 4.00 ± 0.16, N = 9 for V595A; 3.49 ± 0.21, N = 6 for V595K; 3.81 ± 0.07, N = 7 for V595L; 3.48 ± 0.14, N = 7 for V595R). **c,** Effects of different substitutions of V595 on the permeability ratio P_{SCN^-}/P_{Cl^-} (5.47 ± 0.21, N = 28 for WT; 9.96 ± 0.30, N = 9 for V595A; 6.64 ± 0.58, N = 6 for V595K; 7.86 ± 0.37, N = 7 for V595L; 6.30 ± 0.37, N = 7 for V595R). **d**, Permeability ratios determined in bi-ionic conditions for TMEM16A mutants. The exact n values (independent experimental samples from individually recorded HEK293

cells) are given for every experiment. The P-values are generated after a Dunnett's posthoc test following one-way ANOVA. For these multiplicity adjusted P-values, values smaller than 0.0001 cannot be estimated precisely; Prism's documentation suggests this approach is the most rigorous and conservative way to generate a P-value from a multiple comparison test[53].

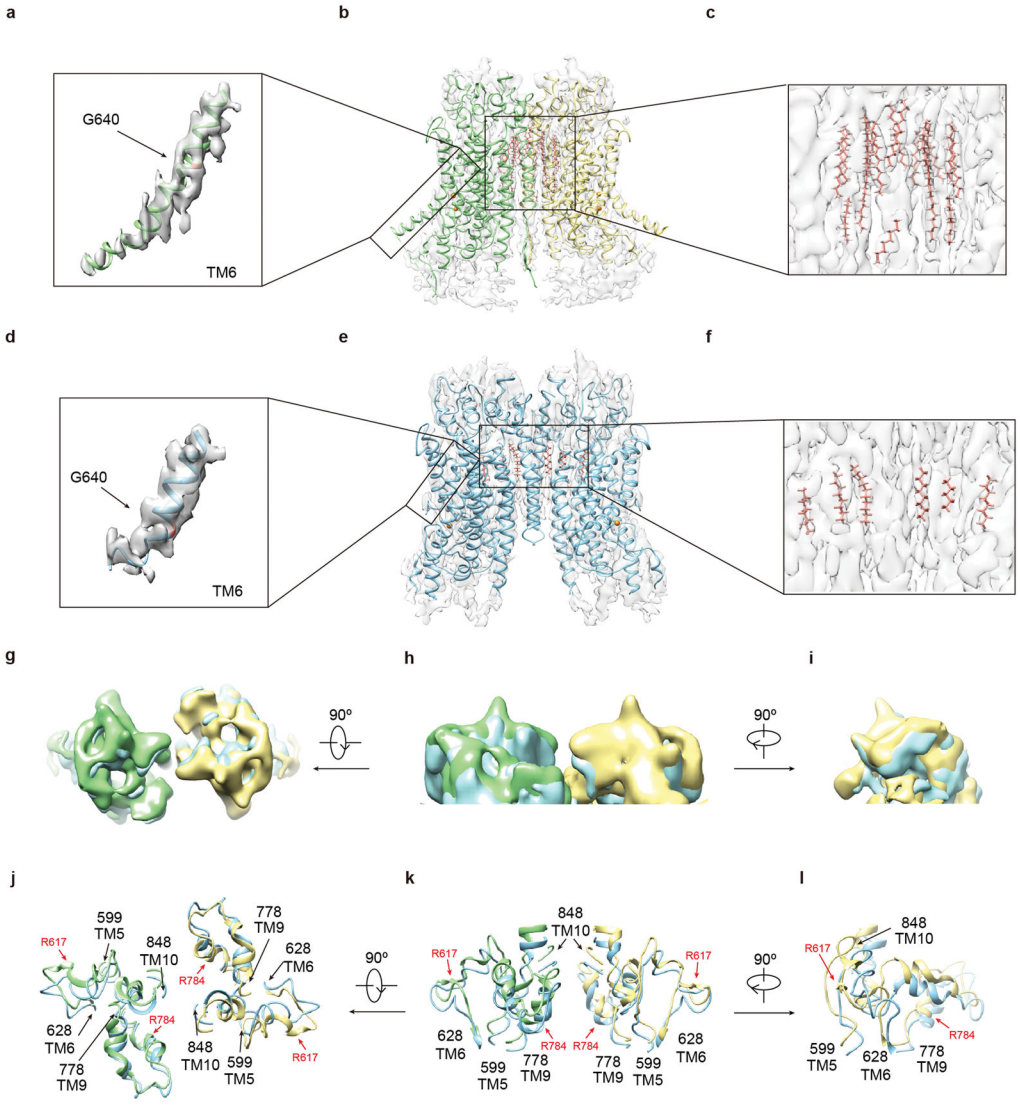

Extended Data Figure 7.

Comparisons of extracellular loops and lipids in nanodisc-resonstituted and LMNG-solubilized TMEM16A. **a–c**, Lipids (in red) in the nanodisc-reconstituted TMEM16A (in green and yellow, overlayed with EM density map in light grey) (**b**, **c**), with helical distortions of TM6 near G640 (**a**). **d–f**, Lipids (in red) in LMNG-solubilized TMEM16A (in blue, overlayed with EM density map in light grey) (**e**, **f**), with the lower half of TM6 beyond G640 disordered and hence absent from the reconstruction (**d**). **g–i**, Extracellular domains of nanodisc-reconstituted TMEM16A (unsharpened, in green and yellow)

overlayed with those of LMNG-solubilized TMEM16A (unsharpened, in blue). **j–l**, Extracellular TM5-TM6 and TM9-TM10 loops in ribbon diagrams for nanodisc-reconstituted TMEM16A (in green and yellow) overlayed with those of LMNG-solubilized TMEM16A (in blue).

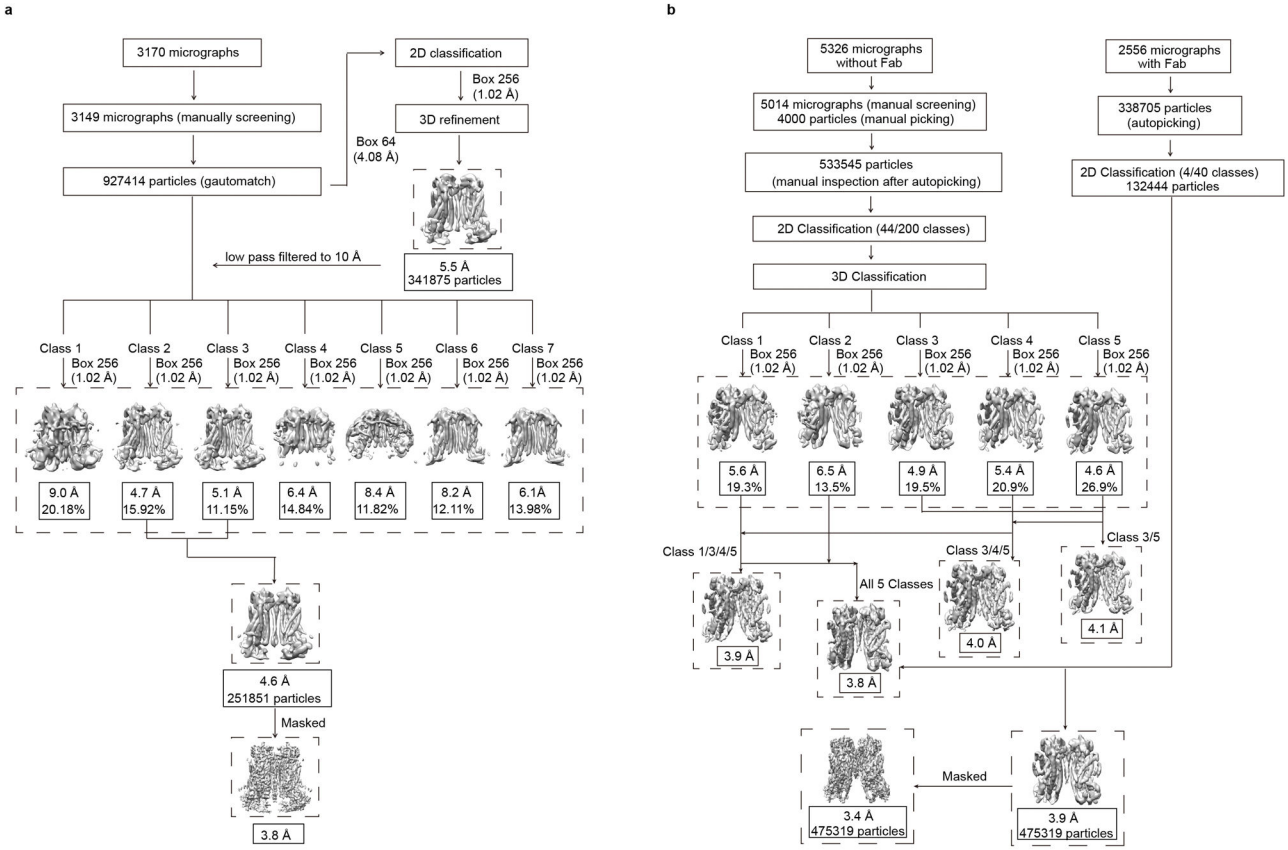

Extended Data Figure 8.

Data processing of TMEM16A in nanodisc (**a**) or LMNG (**b**). **a,** Data processing of nanodisc-reconstituted TMEM16A. Particle picking was performed with Gautomatch with templates from 2D classes from the LMNG dataset and generated 927,414 particles in total. All particles were extracted and binned 4 (pixel size is 4.08 Å) and then 2D classified. 341,875 particles from good 2D classes were used in 3D refinement with an initial model from the LMNG structure low pass filtered to 60 Å, giving rise to a 5.5 Å map. The 5.5 Å map was then low pass filtered to 10 Å as the initial model for 3D classification without applied symmetry for all particles with a 1.02 Å pixel size. Of the seven classes, two classes (15.92% and 11.15% of the 927,414 particles) gave maps with improved resolution (4.7 Å and 5.1 Å respectively) after 3D auto-refinement with C2 symmetry. These two classes were combined together yielding a total of 251,851 particles, and another 3D auto-refinement was run to generate the unmasked map at a resolution of 4.6 Å. The map was then masked to get the final map at resolution of 3.8 Å. **b,** Data processing of LMNG-solubilized TMEM16A. Approximately 4000 particles were manually picked and classified by 2D classification in SAMUEL to generate the templates for automatic particle picking with samautopick.py.

533,545 particles were identified after manually inspection. The crystal structure of nhTMEM16A[10] (PDB: 4WIS) was converted to mrc with e2pdb2mrc.py and low pass filtered to 60 Å as the initial model. 44 of 200 2D classes were used for 3D auto-refinement with C2 symmetry. Since 3D classification failed for further separation, the reported resolution of the final map was 3.8 Å. To reduce anisotropy due to underrepresentation of side views, this dataset was merged with another dataset for Fabs bound to TMEM16A in LMNG. Starting with 338,705 particles from automatic particle picking, 4 of 40 2D classes (132,444 particles) were used for 3D auto-refinement. Then the Fab density for each particle was subtracted. The 132,444 subtracted particles without Fab density were combined with the 342,875 particles from all 5 classes of TMEM16A in LMNG dataset with resolution of 3.8 Å and processed for 3D auto-refinement to generate the unmasked map with resolution of 3.9 Å. This map was then masked to get the final map at resolution of 3.4 Å. Pixel sizes are shown in parenthesis for each class.

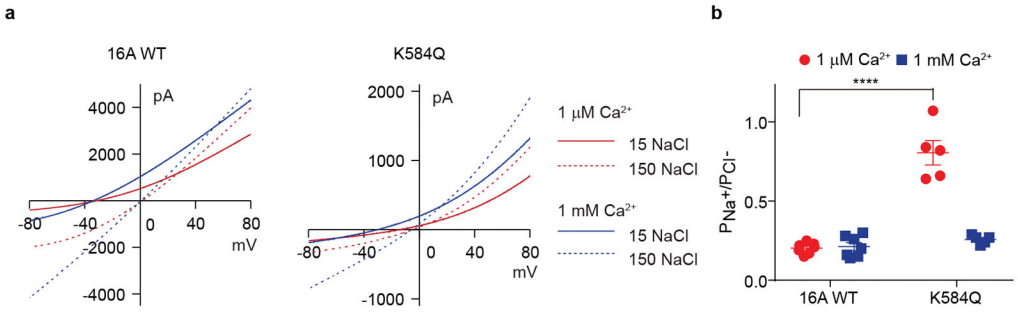

c

	Construct	EC_{50} [Ca2+] (nM) ± SEM	n	P-value
	WT	796 ± 66	10	-
	Δ CTD	178 ± 14	4	< 0.0001
TM4	T533A	1170 ± 145	6	0.4092
	T535A	521 ± 44	5	0.3538
	T537A	1035 ± 117	6	0.8410
	N542A	295 ± 24	10	< 0.0001
	N542D	128 ± 45	4	< 0.0001
	I546A	148 ± 31	6	< 0.0001
	D550A	See Ref. (26)		
	E551A	See Ref. (26)		
TM4-5 Linker	E569A	See Ref. (26)		
	E573A	See Ref. (26)		
TM5	N587A	939 ± 161	13	0.9995
	S588A	1453 ± 122	7	0.0120
	Y589A	192 ± 13	6	< 0.0001
	P591A	673 ± 60	6	0.9947
	I592A	252 ± 17	6	< 0.0001
	V595A	2036 ± 52	7	< 0.0001
TM6	C631A	598 ± 45	7	0.7270
	S635A	See Ref. (13)		
	I637A	See Ref. (13)		
	L639A	2008 ± 63	7	< 0.0001
	Q642A	See Ref. (13)		
TM7	Q705A	1066 ± 81	15	0.4458
	F708A	205 ± 30	8	< 0.0001
	F712A	1177 ± 206	7	0.3823

Extended Data Figure 9.

Multiple open and closed states of TMEM16A calcium-activated chloride channel (CaCC) and involvement of pore-lining residues in channel gating. **a,** Reduction from 150 mM NaCl to 15 mM NaCl in the intracellular solution containing 1 μM or 1 mM Ca^{2+} caused identical shift of reversal potential of wildtype TMEM16A but not K584Q mutant channels in excised inside-out patch held at +80 mV and subjected to a ramp to −80 mV. Repeated independently 8 times for WT with similar results, and 5 times for K584Q with similar results. **b,** The K584Q mutation altered the permeability ratio P_{Na+}/P_{Cl-} at 1 μM but not 1 mM Ca^{2+}. N = 8 for WT, N = 5 for K584Q. **c**, Calcium sensitivity of channel activation of

wildtype and mutant TMEM16A channels (number of independent experiments and P values are given in this table). Permeability ratios for mutants were compared to those of wild-type (WT) using one-way ANOVA followed by the Bonferroni post-hoc test for significance; **** designates $p < 0.0001$; *** designates $p < 0.001$; ** designates $p < 0.005$; data are presented as mean ± SEM.

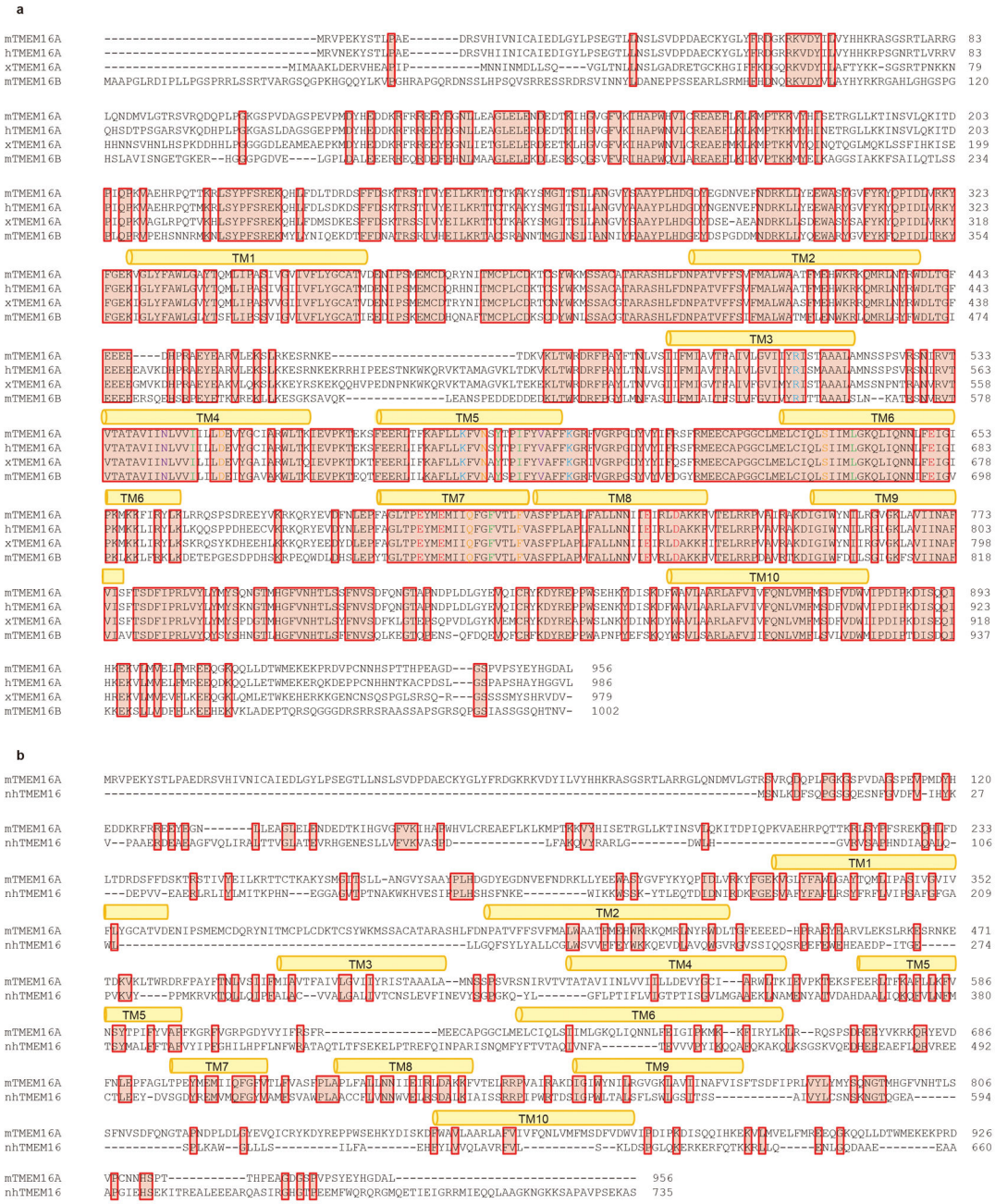

Extended Data Figure 10.

Sequence alignment of TMEM16A homologues. **a,** Sequences of TMEM16A homologues were analyzed by Clustal omega. Conserved residues are highlighted. Transmembrane

helices are indicated above the sequences. The residues that were shown in this study (D550, N587, S635, Q705 and F712) and previous studies (R511, K584 and K599) to be crucial for selectivity are marked in orange and blue respectively. The residues (I546, Y589, I592, L639 and F708) that were shown in this study to be critical for gating are marked in green. The residues (N542 and V595) that contributed to both selectivity and gating property is marked in purple. The residues (E650, E698, E701, E730 and D734) important for Ca^{2+} binding are marked in red. **b,** Sequence alignment of mouse TMEM16A and nhTMEM16. Conserved residues are highlighted. Transmembrane helices of TMEM16A are indicated above the sequence.

Acknowledgments

We thank R. MacKinnon, T. Xiao and W. Wang for advice on protein purification, B. Kobilka and A. Koehl for help on CPM assay, Z. Yu and his colleagues at the HHMI Janelia Cryo-EM Facility for help with data acquisition, and J. Wang at Tsinghua University for discussions on model building. We also thank Peng Jin for help with data presentation and colleagues in our laboratories for discussion. This work was supported by grants from the NIH (R01GM098672 and S100D0020054 to Y.C., R01NS069229 to L.Y.J., R35NS097227 to Y.N.J., R01HL080050 and R01DC007664 to D.L.M., P41CA196276 and P50GM111126 to C.S.C., K99DA041500 to C.J.P.) and from the American Heart Association (M.L.), and by a UCSF Breakthrough Biomedical Research (Y.C.). S. Dang is supported by a Human Frontier Science Program (HFSP) Postdoctoral Fellowship. J.Z. is supported by Banting Postdoctoral Fellowship from the Canadian Institute of Health Research. L.Y.J., Y.N.J. and Y.C. are Investigators with the Howard Hughes Medical Institute.

Uncategorized References

1. Caputo A, et al. TMEM16A, a membrane protein associated with calcium-dependent chloride channel activity. Science (New York, N Y). 2008; 322:590–594.
2. Schroeder BC, Cheng T, Jan YN, Jan LY. Expression cloning of TMEM16A as a calcium-activated chloride channel subunit. Cell. 2008; 134:1019–1029. [PubMed: 18805094]
3. Yang YD, et al. TMEM16A confers receptor-activated calcium-dependent chloride conductance. Nature. 2008; 455:1210–1215. [PubMed: 18724360]
4. Hartzell C, Putzier I, Arreola J. Calcium-activated chloride channels. Annual review of physiology. 2005; 67:719–758.
5. Huang F, Wong X, Jan LY. International Union of Basic and Clinical Pharmacology. LXXXV: Calcium-Activated Chloride Channels. Pharmacol Rev. 2012; 64:1–15. [PubMed: 22090471]
6. Pedemonte N, Galietta LJ. Structure and function of TMEM16 proteins (anoctamins). Physiological reviews. 2014; 94:419–459. [PubMed: 24692353]
7. Oh U, Jung J. Cellular functions of TMEM16/anoctamin. Pflugers Arch. 2016; 468:443–453. [PubMed: 26811235]
8. Lim NK, Lam AK, Dutzler R. Independent activation of ion conduction pores in the double-barreled calcium-activated chloride channel TMEM16A. The Journal of general physiology. 2016; 148:375–392. [PubMed: 27799318]
9. Jeng G, Aggarwal M, Yu WP, Chen TY. Independent activation of distinct pores in dimeric TMEM16A channels. The Journal of general physiology. 2016; 148:393–404. [PubMed: 27799319]
10. Brunner JD, Lim NK, Schenck S, Duerst A, Dutzler R. X-ray structure of a calcium-activated TMEM16 lipid scramblase. Nature. 2014; 516:207–212. [PubMed: 25383531]
11. Brunner JD, Schenck S, Dutzler R. Structural basis for phospholipid scrambling in the TMEM16 family. Curr Opin Struct Biol. 2016; 39:61–70. [PubMed: 27295354]
12. Paulino C, et al. Structural basis for anion conduction in the calcium-activated chloride channel TMEM16A. Elife. 2017; 6
13. Peters CJ, Tien J, Bethel NP, Qi L, Chen T, Wang L, Jan YN, Grabe M, Jan LY. The sixth transmembrane segment as the primary gating machineray of the TMEM16A calcium-activated chloride channel. 2017 Submitted.

14. Scudieri P, Sondo E, Caci E, Ravazzolo R, Galietta LJ. TMEM16A-TMEM16B chimaeras to investigate the structure-function relationship of calcium-activated chloride channels. Biochem J. 2013; 452:443–455. [PubMed: 23570556]
15. Scudieri P, Musante I, Gianotti A, Moran O, Galietta LJ. Intermolecular Interactions in the TMEM16A Dimer Controlling Channel Activity. Sci Rep. 2016; 6:38788. [PubMed: 27929144]
16. Alexandrov AI, Mileni M, Chien EY, Hanson MA, Stevens RC. Microscale fluorescent thermal stability assay for membrane proteins. Structure. 2008; 16:351–359. [PubMed: 18334210]
17. Ashok Y, Jaakola VP. Nanodisc-Tm: Rapid functional assessment of nanodisc reconstituted membrane proteins by CPM assay. MethodsX. 2016; 3:212–218. [PubMed: 27054097]
18. Duriseti S, et al. Antagonistic anti-urokinase plasminogen activator receptor (uPAR) antibodies significantly inhibit uPAR-mediated cellular signaling and migration. The Journal of biological chemistry. 2010; 285:26878–26888. [PubMed: 20501655]
19. Wu S, et al. Fabs enable single particle cryoEM studies of small proteins. Structure. 2012; 20:582–592. [PubMed: 22483106]
20. Smart OS, Neduvelil JG, Wang X, Wallace BA, Sansom MS. HOLE: a program for the analysis of the pore dimensions of ion channel structural models. J Mol Graph. 1996; 14:354–360. 376. [PubMed: 9195488]
21. Whitlock JM, Hartzell HC. A Pore Idea: the ion conduction pathway of TMEM16/ANO proteins is composed partly of lipid. Pflugers Arch. 2016; 468:455–473. [PubMed: 26739711]
22. Whitlock JM, Hartzell HC. Anoctamins/TMEM16 Proteins: Chloride Channels Flirting with Lipids and Extracellular Vesicles. Annual review of physiology. 2017; 79:119–143.
23. Yu K, et al. Identification of a lipid scrambling domain in ANO6/TMEM16F. Elife. 2015; 4:e06901. [PubMed: 26057829]
24. Jiang TYK, Hartzell HC, Tajkhorshid E. Lipids and ions traverse the membrane by the same physical pathway in the nhTMEM16 scramblase. Elife. 2017 in press.
25. Peters CJ, et al. Four basic residues critical for the ion selectivity and pore blocker sensitivity of TMEM16A calcium-activated chloride channels. Proceedings of the National Academy of Sciences of the United States of America. 2015; 112:3547–3552. [PubMed: 25733897]
26. Tien J, et al. A comprehensive search for calcium binding sites critical for TMEM16A calcium-activated chloride channel activity. Elife. 2014; 3
27. Yu K, Duran C, Qu Z, Cui YY, Hartzell HC. Explaining calcium-dependent gating of anoctamin-1 chloride channels requires a revised topology. Circ Res. 2012; 110:990–999. [PubMed: 22394518]
28. Yang H, et al. TMEM16F forms a Ca2+-activated cation channel required for lipid scrambling in platelets during blood coagulation. Cell. 2012; 151:111–122. [PubMed: 23021219]
29. Goehring A, et al. Screening and large-scale expression of membrane proteins in mammalian cells for structural studies. Nature protocols. 2014; 9:2574–2585. [PubMed: 25299155]
30. Whicher JR, MacKinnon R. Structure of the voltage-gated K(+) channel Eag1 reveals an alternative voltage sensing mechanism. Science (New York, N Y. 2016; 353:664–669.
31. Gao Y, Cao E, Julius D, Cheng Y. TRPV1 structures in nanodiscs reveal mechanisms of ligand and lipid action. Nature. 2016; 534:347–351. [PubMed: 27281200]
32. Mastronarde DN. Automated electron microscope tomography using robust prediction of specimen movements. J Struct Biol. 2005; 152:36–51. [PubMed: 16182563]
33. Liao M, Cao E, Julius D, Cheng Y. Structure of the TRPV1 ion channel determined by electron cryo-microscopy. Nature. 2013; 504:107–112. [PubMed: 24305160]
34. Frank J, et al. SPIDER and WEB: processing and visualization of images in 3D electron microscopy and related fields. J Struct Biol. 1996; 116:190–199. [PubMed: 8742743]
35. Zheng SQ, et al. MotionCor2: anisotropic correction of beam-induced motion for improved cryo-electron microscopy. Nature methods. 2017; 14:331–332. [PubMed: 28250466]
36. Rohou A, Grigorieff N. CTFFIND4: Fast and accurate defocus estimation from electron micrographs. J Struct Biol. 2015; 192:216–221. [PubMed: 26278980]
37. Zhang K. Gctf: Real-time CTF determination and correction. J Struct Biol. 2016; 193:1–12. [PubMed: 26592709]

38. Scheres SH. RELION: implementation of a Bayesian approach to cryo-EM structure determination. J Struct Biol. 2012; 180:519–530. [PubMed: 23000701]
39. Tang G, et al. EMAN2: an extensible image processing suite for electron microscopy. J Struct Biol. 2007; 157:38–46. [PubMed: 16859925]
40. Scheres SH, Chen S. Prevention of overfitting in cryo-EM structure determination. Nature methods. 2012; 9:853–854. [PubMed: 22842542]
41. Kucukelbir A, Sigworth FJ, Tagare HD. Quantifying the local resolution of cryo-EM density maps. Nature methods. 2014; 11:63–65. [PubMed: 24213166]
42. Emsley P, Lohkamp B, Scott WG, Cowtan K. Features and development of Coot. Acta Crystallogr D Biol Crystallogr. 2010; 66:486–501. [PubMed: 20383002]
43. Trabuco LG, Villa E, Mitra K, Frank J, Schulten K. Flexible fitting of atomic structures into electron microscopy maps using molecular dynamics. Structure. 2008; 16:673–683. [PubMed: 18462672]
44. Adams PD, et al. PHENIX: a comprehensive Python-based system for macromolecular structure solution. Acta Crystallogr D Biol Crystallogr. 2010; 66:213–221. [PubMed: 20124702]
45. Brown A, et al. Tools for macromolecular model building and refinement into electron cryo-microscopy reconstructions. Acta Crystallogr D Biol Crystallogr. 2015; 71:136–153. [PubMed: 25615868]
46. Chen VB, et al. MolProbity: all-atom structure validation for macromolecular crystallography. Acta Crystallogr D Biol Crystallogr. 2010; 66:12–21. [PubMed: 20057044]
47. Barad BA, et al. EMRinger: side chain-directed model and map validation for 3D cryo-electron microscopy. Nature methods. 2015; 12:943–946. [PubMed: 26280328]
48. DeLano, WL. The PyMOL molecular graphics system on world wide web. 2002. http://www.pymol.org
49. Saxton WO, Baumeister W. The correlation averaging of a regularly arranged bacterial cell envelope protein. J Microsc. 1982; 127:127–138. [PubMed: 7120365]
50. van Heel M, Stoffler-Meilicke M. Characteristic views of E. coli and B. stearothermophilus 30S ribosomal subunits in the electron microscope. EMBO J. 1985; 4:2389–2395. [PubMed: 3908096]
51. Pettersen EF, et al. UCSF Chimera--a visualization system for exploratory research and analysis. J Comput Chem. 2004; 25:1605–1612. [PubMed: 15264254]
52. Rosenthal PB, Henderson R. Optimal determination of particle orientation, absolute hand, and contrast loss in single-particle electron cryomicroscopy. J Mol Biol. 2003; 333:721–745. [PubMed: 14568533]
53. Wright SP. Adjusted P-values for simultaneous inference. Biometrics. 1992; 48:1005–1013.

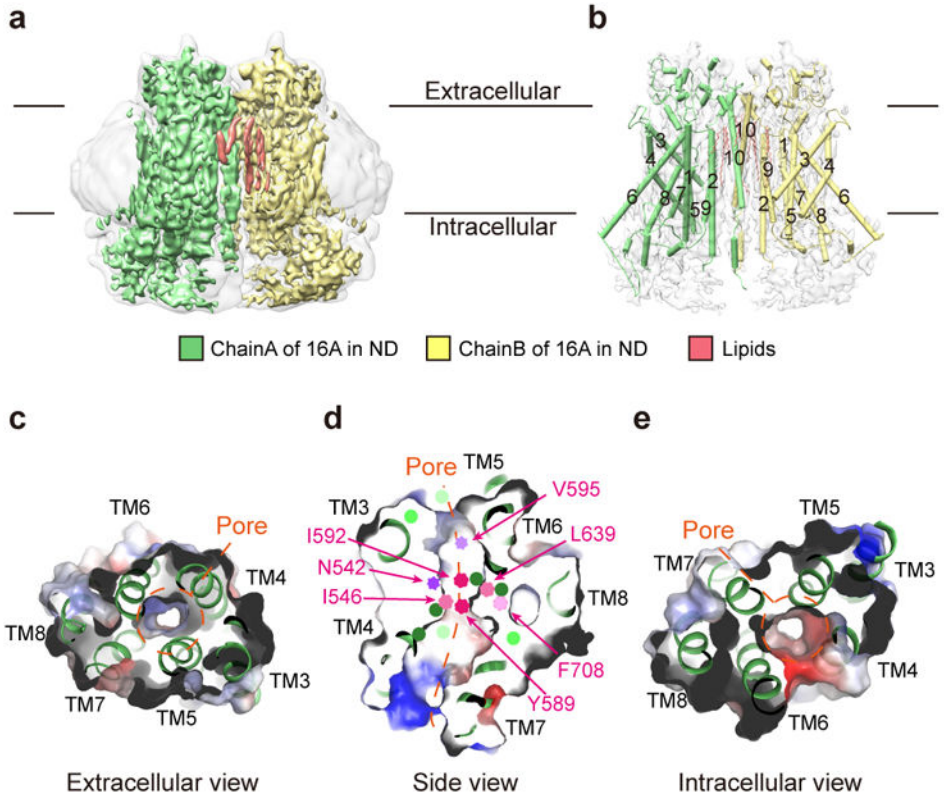

Figure 1.

Structure of TMEM16A in nanodiscs. **a**, EM density map of TMEM16A (sharpened, green and yellow) over a density map with a lower threshold (unsharpened) in light grey for nanodiscs. **b**, TM1–10 overlayed with EM density map of TMEM16A (sharpened, light grey). **c–e**, The channel pore (marked in orange) lined with N542 and V595 (in purple) that affect both anion selectivity and channel gating, five other residues that affect channel gating (in magenta) (see Fig. 4) and eight other residues that affect ion selectivity (in green) (see Fig. 3).

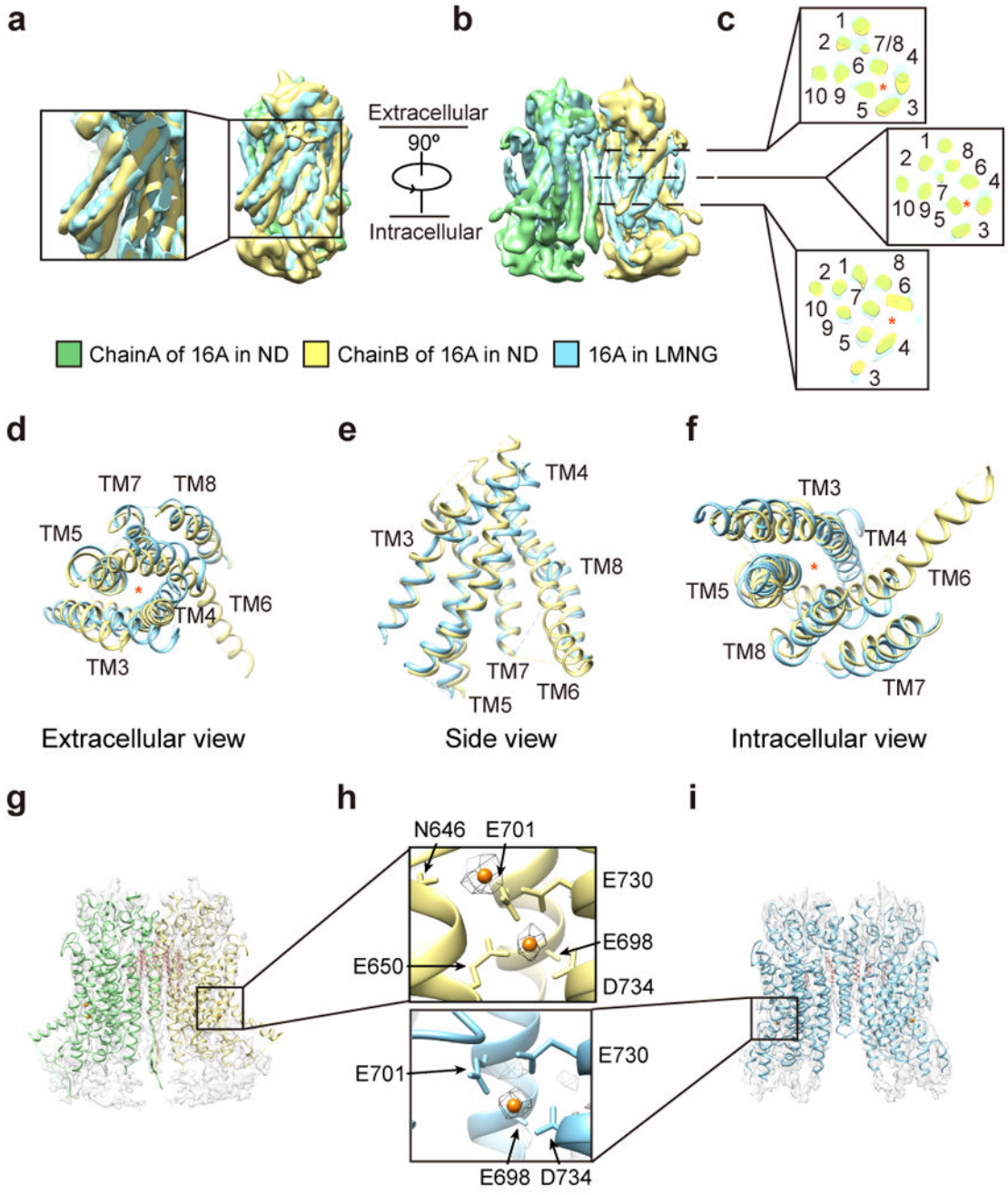

Figure 2.

Differences in pore-lining helices and Ca^{2+} ion binding in the two structures. **a–b**, Density map of nanodisc-reconstituted TMEM16A (unsharpened, green and yellow) overlayed with that of LMNG-solubilized TMEM16A (unsharpened, blue). **c**, Conformational differences of pore-lining helices. **d–f**, Comparisons of TM3–8 around the pore (orange asterisk) in two structures. **g–i**, Two Ca^{2+} ions (orange spheres) coordinated by five acidic residues and one asparagine (N646) in nanodisc-reconstituted TMEM16A (**g**, **h**) versus one Ca^{2+} ion surrounding by four acidic residues in LMNG-solubilized TMEM16A (**i**, **h**) (Methods).

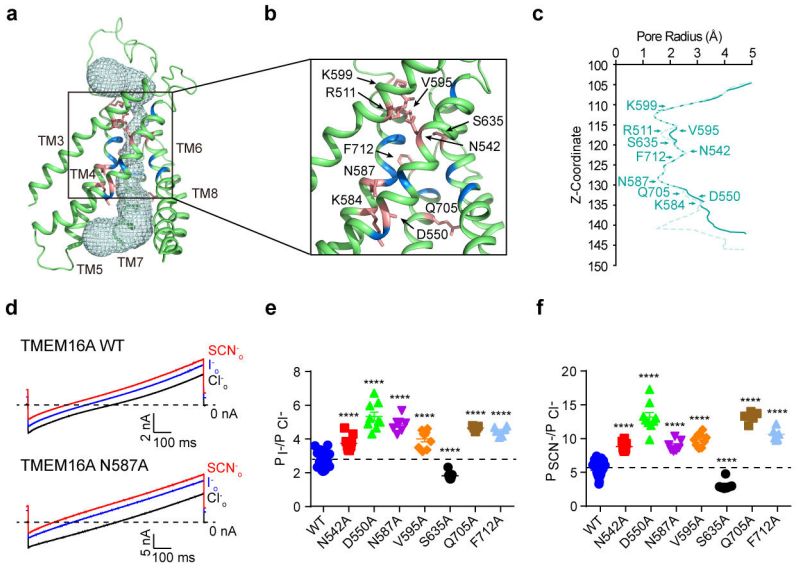

Figure 3.

The pore of TMEM16A in nanodiscs. **a, b,** The solvent-accessible (blue mesh) pore lined with residues important for anion selectivity (salmon sticks, labeled in **b**) and those without detected effects (blue backbone) (N and P values are given in Methods and Extended Data Fig. 6d). **c**, Pore radius along the Z axis. For those residues not completely resolved, a solid line and a dotted line based on positioning two rotamers bracket the pore radius estimate. **d,** Representative recordings under bi-ionic conditions (repeated 7 times with similar results). **e–f,** Permeability ratios for iodide/chloride (**e**), or thiocyanate/chloride (**f**) (Methods) assessed via one-way ANOVA followed by Bonferroni post-hoc test; **** designates $p < 0.0001$; mean ± SEM.

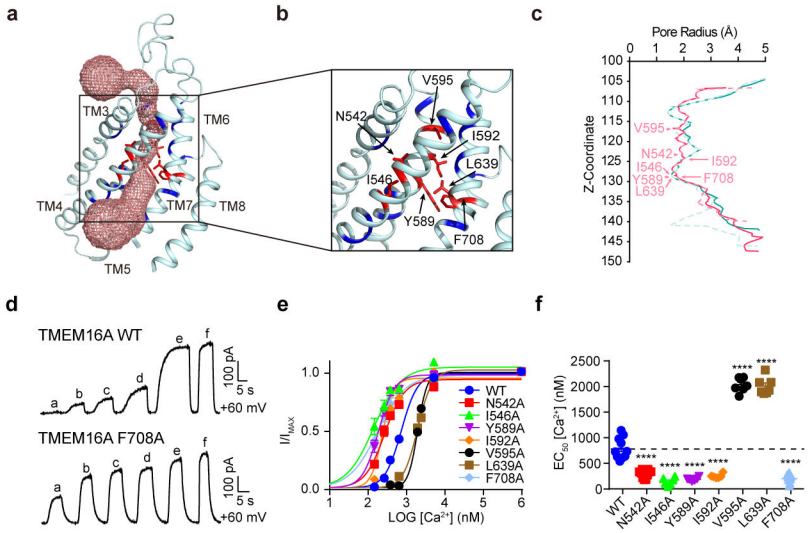

Figure 4.

The pore of LMNG-solubilized TMEM16A. **a**, **b**, The solvent-accessible (red mesh) pore lined with residues affecting channel gating (red sticks, labeled in **b**) and those without effects (dark blue backbone). **c**, Pore radius (salmon; pore radius of nanodisc-reconstituted TMEM16A in green) along the Z axis. For those residues not completely resolved, a solid line and a dotted line bracket the pore radius estimate (Methods). **d,** Representative recordings of inside-out patch exposed to increasing Ca^{2+} levels (repeated 8 times with similar results). **e,** Normalized currents fit to the Hill equation. The Hill coefficient for L639A is 2.34 ± 0.11. **f,** EC_{50} values (N and P values are given in Methods and Extended Data Fig. 9c) compared via one-way ANOVA followed by Bonferroni post-hoc test; **** designates $p < 0.0001$; mean ± SEM.

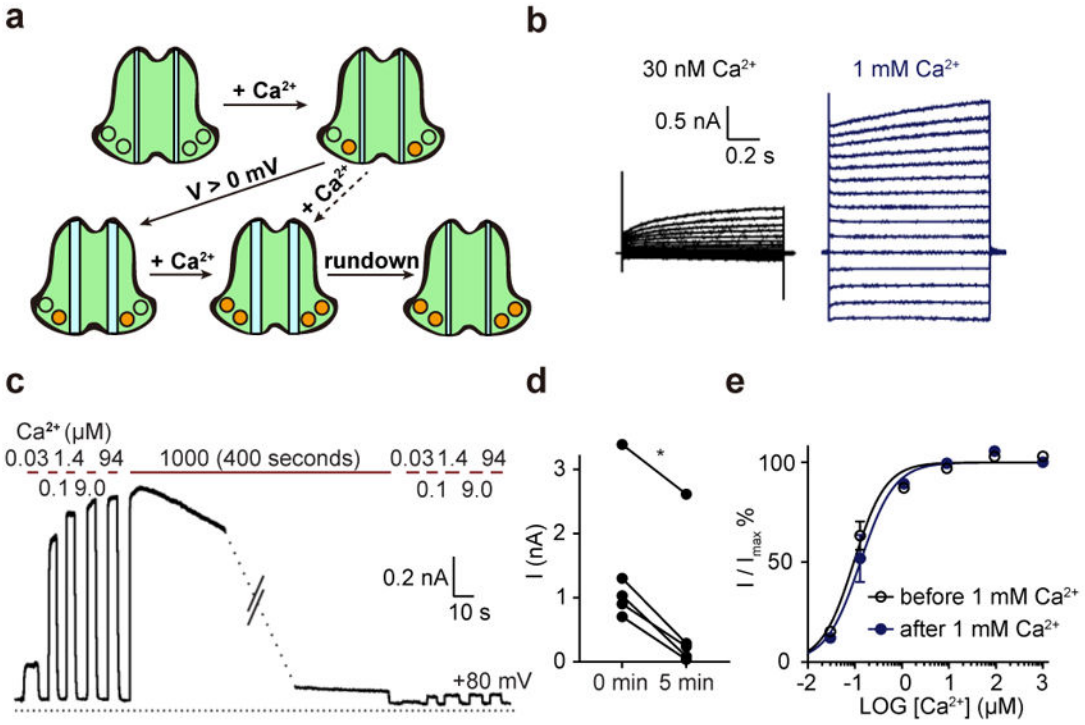

Figure 5.

Different conformations of TMEM16A. **a,** Schematic showing the dimeric CaCC in a calcium-free closed conformation (top left panel), CaCC with single calcium occupancy that remains closed (top right panel) until depolarization causes it to open (bottom left panel), CaCC with double calcium occupancy that opens in a voltage-independent manner (bottom middle panel), and channel rundown following prolonged activation (bottom right panel). **b–e,** TMEM16A with C-terminal truncation yielded voltage-dependent current in 30 nM Ca^{2+} but voltage-independent current in 1 mM Ca^{2+} (**b**), while prolonged activation causes channel rundown (**c**) (N = 5; p = 0.03) (**d**) without significant change in Ca^{2+} sensitivity (EC_{50} = 0.11 ± 0.02 μM before exposure to 1 mM Ca^{2+}, EC_{50} = 0.15 ± 0.04 μM after exposure to EC_{50} = 0.15 ± 0.04 μM, p = 0.13, N = 4, two-tailed Wilcoxon test) (**e**); mean ± SEM.